Article

Immunity

CCR7^{+} activated dendritic cells are essential for spontaneous and immunotherapy-driven anti-tumor immunity

Graphical abstract

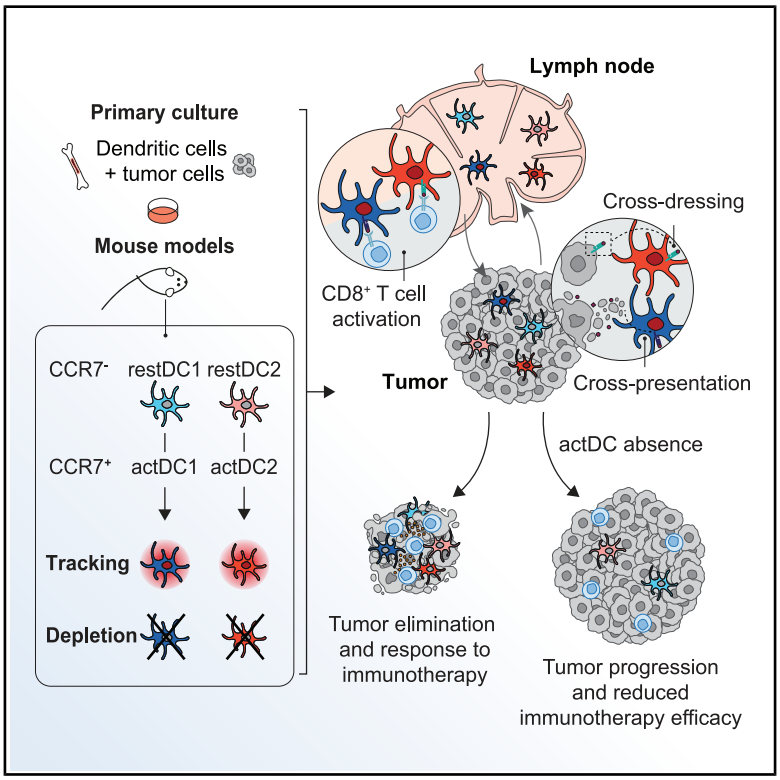

Authors

Maria A. Koufaki, Erin Richardson, Eduardo Bonavita, ..., Andrew S. MacDonald, Natalia Moncaut, Santiago Zelenay

Correspondence

santiago.zelenay@cruk.manchester.ac.uk

In brief

Dendritic cells (DCs) can acquire distinct functional states. To examine how different DC states orchestrate anti-tumor immunity, Koufaki et al. develop mouse models to label and ablate CCR7^{+} DCs and find that this activation state is essential for tumor control by uniquely priming tumor-specific cytotoxic T lymphocytes (CTLs), sustaining their function and enabling responses to immunotherapy.

Highlights

- *Ccr7*$^{LSL\text{-}mScarlet\text{-}I}$ and *Ccr7*$^{LSL\text{-}DTR}$ mice enable conditional labeling or ablation of actDCs
- actDCs uniquely mediate cDC-driven stimulation of tumor-specific CTLs
- actDC1s prime CTLs via cross-presentation, whereas actDC2s use cross-dressing
- actDCs enable responses to checkpoint blockade and adoptive T cell therapy

Koufaki et al., 2026, Immunity *59*, 2282–2298
August 11, 2026
https://doi.org/10.1016/j.immuni.2026.07.002

CellPress

CellPress
OPEN ACCESS

Immunity

Article

CCR7^{+} activated dendritic cells are essential for spontaneous and immunotherapy-driven anti-tumor immunity

Maria A. Koufaki,[1] Erin Richardson,[1,12] Eduardo Bonavita,[1,10,12] Richard Reeves,[2] Agrin Moeini,[1] Shih-Chieh Chiang,[1] Antonia Banyard,[3] Massimo Russo,[1] Charles H. Earnshaw,[1,4] Charlotte R. Bell,[1] Eimear Flanagan,[1] Victoria S. Pelly,[1] Laetitia Nebot-Bral,[1] Anna Pidoux,[1] Poppy Dunn,[1] Sudhakar Sahoo,[2] Sandrine Henri,[5] Bernard Malissen,[6,7] Andrew S. MacDonald,[8,11] Natalia Moncaut,[9] and Santiago Zelenay[1,8,13,*]

[1]Cancer Inflammation and Immunity, Cancer Research UK Manchester Institute, The University of Manchester, Manchester, UK
[2]Computational Biology Support, Cancer Research UK Manchester Institute, The University of Manchester, Manchester, UK
[3]Flow Cytometry, Cancer Research UK Manchester Institute, The University of Manchester, Manchester, UK
[4]Dermatology Centre, Northern Care Alliance NHS Foundation Trust & Division of Musculoskeletal and Dermatological Sciences, Manchester NIHR Biomedical Research Centre, Manchester Academic Health Science Centre, The University of Manchester, Manchester, UK
[5]Centre d'Etude des Pathologies Respiratoires, INSERM, UMR 1100, Université de Tours, Tours, France
[6]Centre d'Immunologie de Marseille-Luminy, INSERM, CNRS, Aix Marseille Université, Marseille, France
[7]Centre d'Immunophénomique, INSERM, CNRS, PHENOMIN, Celphedia, Aix Marseille Université, Marseille, France
[8]Lydia Becker Institute of Immunology and Inflammation, The University of Manchester, Manchester, UK
[9]Genome Editing and Mouse Models, Cancer Research UK Manchester Institute, The University of Manchester, Manchester, UK
[10]Present address: Department of Biomedical Sciences, Humanitas University, Laboratory of Cellular and Molecular Oncoimmunology, IRCCS Humanitas Research Hospital, Milan, Italy
[11]Present address: Institute of Immunology and Infection Research, University of Edinburgh, Edinburgh, UK
[12]These authors contributed equally
[13]Lead contact
*Correspondence: santiago.zelenay@cruk.manchester.ac.uk
https://doi.org/10.1016/j.immuni.2026.07.002

SUMMARY

Single-cell transcriptomics identifies a convergent activation state of conventional dendritic cells (cDCs) shared by type 1 and type 2 cDCs (cDC1s and cDC2s). These activated DCs (actDCs) are characterized by co-expression of T cell-stimulating and inhibitory molecules. Here, we examined the functional contribution of actDCs to anti-tumor immunity by developing mouse models that leverage CCR7 expression to conditionally label or ablate actDCs. The capacity of cDCs to stimulate tumor-specific cytotoxic T lymphocytes (CTLs) was restricted to the actDC state. cDC1- and cDC2-derived actDCs supported CTL priming through cross-presentation and cross-dressing, respectively, with the latter occurring in a cancer type-dependent manner. actDCs were required for the activation of naive CTLs in tumor-draining lymph nodes and for sustaining effector CTL function within tumors. Consequently, ablation of actDCs impaired spontaneous tumor control and responses to immune checkpoint blockade or adoptive T cell therapy. Thus, the actDC state emerges as a critical determinant of cDC-mediated anti-tumor immunity.

INTRODUCTION

Conventional dendritic cells (cDCs) are central mediators of natural and therapy-induced immune responses against tumors, owing to their unique ability to take up tumor material and migrate to draining lymph nodes (dLNs) to stimulate naive tumor-specific CD4^{+} and CD8^{+} T cells.[1–4] Beyond this priming function, cDCs also play key roles at the tumor site by attracting and promoting T cell activation locally.[5–10] Among cDC subsets, type 1 conventional cDCs (cDC1s) are well-established orchestrators of cytotoxic T lymphocyte (CTL)-mediated anti-tumor responses[2,5,11,12] due to their distinctive capacity to cross-present cancer cell-derived antigens on major histocompatibility complex class I (MHC-I) molecules.[5,12–17] Accordingly, tumor-infiltrating cDC1 abundance correlates with favorable patient prognosis and response to immune checkpoint blockade (ICB) therapy.[3,18–23] The contribution of cDC2s to CTL-mediated tumor immunity is less well defined. Cross-dressing represents a mechanism through which cDC2s can prime tumor-reactive CTLs by acquiring preformed peptide-MHC-I complexes from cancer cells.[24–26]

Single-cell transcriptomic analyses of tumor-infiltrating leukocytes identify a cDC population that clusters independently of cDC1s and cDC2s, infiltrates multiple cancer types in mice and

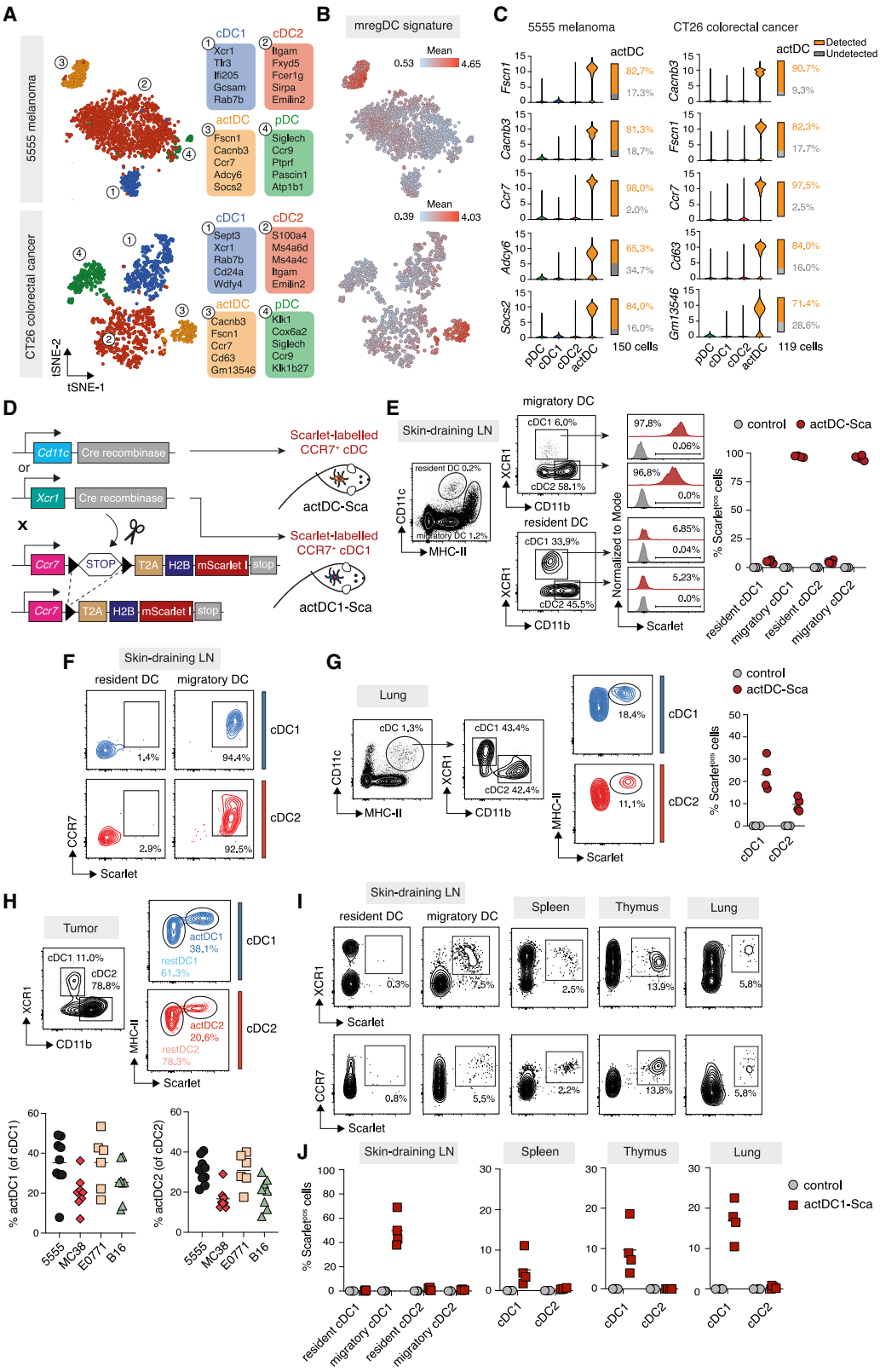

Figure 1. A conditional reporter mouse model enables labeling of CCR7$^+$ activated DCs

(A) t-SNE plots of intratumoral DCs from single-cell RNA sequencing of sorted CD45$^+$ cells from 5555 or CT26 tumors. Different clusters—cDC1 (blue), cDC2 (red), actDC (orange), and pDC (green)— alongside the top five markers characterizing each cluster are shown.

(legend continued on next page)

humans, and is characterized by high co-expression of T cell-stimulating molecules (CCR7, IL-12, CD80, CD86, and CD40) alongside immune inhibitory molecules including PD-L1.[27–31] Their dual expression profile underlies their designation as "mature DCs enriched in immunoregulatory molecules" (mregDCs),[32–34] although the terms mature DCs (mDCs), migratory DCs (migDCs), DC3s, or CCR7^{+} DCs[8,24,27–29,31,32,35] are also in use. Transcriptional and phenotypic analysis indicates that these cells represent a convergent activation state arising from both cDC1s and cDC2s[27,30,32–34,36] and are henceforth referred to as activated DCs (actDCs). However, their overall contribution to anti-tumor immunity remains poorly understood, with evidence for both immune-stimulating and -restraining functions.[33,37–41] A major challenge in defining their contribution is that actDCs are typically scarce, representing a minority of the whole cDC compartment. Moreover, experimental models to unequivocally identify and distinguish cDC1-derived and cDC2-derived actDCs (termed actDC1s and actDC2s, respectively) or to conditionally ablate them and determine the impact of their absence are lacking.

Here, we described the development of two new genetically engineered mouse lines using intersectional genetics to enable either specific labeling, imaging, and isolation of actDCs or their acute depletion. Using these models, we uncovered distinctive functional features of actDC1s and actDC2s. Furthermore, we formally demonstrated the essential contribution of the actDC state to CTL-dependent tumor control, both in spontaneous settings and in response to ICB or adoptive T cell therapy (ACT).

RESULTS

Mouse strain to conditionally label CCR7^{+} actDCs

Transcriptomic profiling of CD45^{+} cells infiltrating tumors formed by 5555 Braf^{V600E}-driven melanoma or CT26 colorectal carcinoma cells revealed a transcriptionally distinct cDC cluster (Figures 1A, S1A, and S1B; Table S1). Within the overall DC cluster, we identified four independent populations: cDC1s, cDC2s, plasmacytoid DCs (pDCs), and a fourth cDC cluster that, due to the lack of common lineage-defining markers, could not be ascribed to any of these lineages. Cells within this fourth cluster showed selectively high mRNA levels of *Ccr7*, *Fscn1*, *Cd80*, *Cd40*, *Socs2*, il*12b*, *Cd274*, *Ccl17*, *Cxcl16*, and *Ccl22*, among others, consistent with the previously described mregDC, migDC, mDC, CCR7^{+} DC, or DC3 signatures (Figures 1B and S1C–S1E).[8,24,28,29,31–33,35] Regulatory network analysis revealed high specificity scores for the *Stat4*, *Nfkb2*, and *Nfat5* transcription factors within this cluster (Figure S1F), all of which have been linked to DC activation.[20,42,43] Trajectory inference and RNA velocity analysis further pinpointed this cluster as a differentiated cDC state (Figure S1G) acquired by both cDC1s and cDC2s. Indeed, flow cytometry analysis showed that CCR7^{+} cDCs fell within cDC1 or cDC2 gates, albeit expressing lower surface levels of lineage-defining markers than their CCR7^{-} counterparts (Figures S1H and S1I). They also showed elevated surface expression of CD40, CD86, CD63, PD-L1, MHC-I, and MHC-II (Figure S1I). Together, these data established that this transcriptionally distinct cluster represents a convergent activation state shared by cDC1s and cDC2s,[27,30,32–34,36,44] here termed actDCs (actDC1s or actDC2s according to their lineage of origin).

The functional characterization of actDCs has been hindered by their scarcity. Moreover, most markers that distinguish actDCs from their non-activated resting counterparts (henceforth restDC1s and restDC2s) are also expressed by other cell types, requiring their identification by a combination of markers. To overcome these limitations, we developed a genetically engineered mouse line that would enable selective labeling, tracking, and isolation of actDCs. Among the top genes defining the actDC cluster in both tumor models, *Ccr7* was detected in virtually all actDCs but was absent from the other cDC clusters (Figures 1C and S1B). We therefore generated a mouse line encoding the fluorescent protein mScarlet-I (Scarlet) at the 3′ end of the *Ccr7* gene, preceded by a loxP-STOP-loxP (LSL) cassette (Figure 1D and STAR Methods). This design enables Cre-dependent, CCR7-transcription-coupled Scarlet expression, allowing conditional labeling of actDCs according to the Cre driver used.

Crossing to the CD11c-Cre driver[45] generated *Itgax*^{Cre} *Ccr7*$^{LSL\text{-}mScarlet\text{-}I}$ (actDC-Sca) animals (Figure 1D), in which all CCR7^{+} CD11c^{+} cells were expected to express Scarlet. Accordingly, CCR7^{+} migratory (CD11c^{low} MHC-II^{high}) cDC1s and cDC2s in skin-dLNs showed bright Scarlet fluorescence, whereas LN-resident cDCs and control Cre-negative animals were Scarlet^{neg} (Figures 1E and 1F). In the spleen, which lacks afferent lymphatic vessels, only ∼4%–8% of cDC1s and cDC2s expressed Scarlet (Figure S2A), while in the lung, Scarlet^{pos} cells represented ∼25% of cDC1s and ∼10% of cDC2s (Figure 1G). To assess the integrity of the targeted *Ccr7* locus, we evaluated

(B) t-SNE plots of intratumoral DCs from 5555 or CT26 tumors colored by expression score of the mregDC signature.[33]
(C) Violin plots showing expression levels of the top five markers characterizing actDCs in 5555 or CT26 tumors and frequency of gene expression within the actDC cluster per tumor type.
(D) Schematic of the design strategy to generate actDC-Sca and actDC1-Sca mice.
(E) Representative gating strategy of cDCs in skin-draining LNs of naive mice. The frequency of Scarlet^{pos} cells in cDC subsets present in LNs of actDC-Sca (dark red) or control (gray) mice is shown (n = 3–4 mice/group, representative of two independent experiments).
(F) Representative contour plots demonstrating expression of Scarlet and CCR7 in total cDC1s and cDC2s in skin-draining LNs.
(G) Representative gating strategy of cDCs in the lung of naive mice. The frequency of Scarlet^{pos} cells in cDC subsets present in the lung of actDC-Sca (dark red) or control (gray) mice is shown (n = 3–4 mice/group, representative of two independent experiments).
(H) Representative gating strategy of cDC populations in B16 tumors. Frequency of Scarlet^{pos} cells within intratumoral cDC1s and cDC2s of four syngeneic tumor models within 10 days of growth is shown (n = 6–9 mice/group, pooled from two independent experiments). One million cancer cells were injected subcutaneously in the flank of actDC-Sca mice.
(I) Representative contour plots demonstrating expression of XCR1, Scarlet, and CCR7 in total DCs across actDC1-Sca tissues.
(J) Frequency of Scarlet^{pos} cells in cDC populations present in lymphoid tissues and lung of actDC1-Sca or control mice (n = 3–4 mice/group).
Data are presented as individual values (each dot represents a single mouse), with the mean indicated.
See also Figures S1 and S2.

the migration of FLT3L bone marrow-derived DCs (BMDCs) toward CCL21. CCR7^{+} cDC1s and cDC2s generated from actDC-Sca or control animals migrated equally well toward CCL21 (Figure S2B), indicating that targeting did not alter CCR7 function.

Next, we assessed Scarlet expression within tumor-infiltrating cDCs using four independent syngeneic cancer models implanted in actDC-Sca mice (Figures 1H, S2C, and S2D). Scarlet^{pos} cDCs were found in all models, representing ~20%–40% of both cDC1s and cDC2s depending on tumor type (Figure 1H). Phenotypic analysis confirmed elevated MHC-II, PD-L1, and PD-L2 on Scarlet^{pos} cDC1s and cDC2s, with IL-12 restricted to Scarlet^{pos} cDC1s (Figure S2E). Consistent with activation-associated loss of lineage-defining markers,[44,46–48] surface levels of XCR1 on cDC1s and CD11b on cDC2s were lower in Scarlet^{pos} than in Scarlet^{neg} cells (Figure S2E). Scarlet expression was also detected in CCR7^{+} B and T cells (Figures S2F–S2H), consistent with the known physiological activity of CD11c-Cre in lymphocytes.[49,50] After gating out these Scarlet^{pos} lymphocytes, the actDC-Sca line selectively identifies CCR7^{+} actDCs within the cDC compartment.

The actDC1-Sca reporter enables visualization of actDC1s in lymphoid and non-lymphoid organs and tumors

We next utilized an Xcr1-Cre driver[51] to generate *Xcr1*$^{Cre\text{-}mTFP1}$ *Ccr7*$^{LSL\text{-}mScarlet\text{-}I}$ mice (actDC1-Sca) such that only actDC1s would express Scarlet (Figure 1D). Mice with evidence of germline Cre activity (a known feature of Xcr1-Cre driver lines[51–53]) were identified by blood cell phenotyping and excluded (see STAR Methods). In validated actDC1-Sca animals, bright Scarlet expression was observed exclusively within CCR7^{+} cDC1s across lymphoid and non-lymphoid organs, with no signal in resident DCs or other immune populations (Figures 1I, 1J, and S2F). Thus, in contrast to actDC-Sca mice, in which incomplete lineage restriction resulted in Cre activity in CCR7^{+} B and T cells, the actDC1-Sca strain enabled exclusive labeling of actDC1s.

Using this reporter, we mapped the spatial distribution of actDC1s across tissues and tumors via microscopy (Figure S2I). In skin-dLNs and spleen, Scarlet^{pos} cells were enriched in the T cell zone area and sparse within B cell follicles or splenic red pulp (Figures 2A and 2B).[54,55] In the thymus, Scarlet^{pos} cells were observed in medullary regions but were rarely found in the cortex (Figures 2A and 2B).[44] In non-lymphoid organs, actDC1s were dispersed throughout the lung and liver parenchyma but were absent across multiple regions of the brain (Figures 2A, 2B, S2J, and S2K). In tumors, actDC1s were predominantly located within 30 μm of CD31^{+} blood vessels (Figures 2C and 2D)[6,39,56] and were far less abundant than CD8^{+} T cells (Figure 2E). Although actDC1s formed clusters with CD8^{+} T cells, approximately half were located more than 30 μm away from CD8^{+} T cells (Figures 2C and 2F). Together, these data established that the *Ccr7*$^{LSL\text{-}mScarlet\text{-}I}$ reporter line enables labeling of either all actDCs or selectively of actDC1s, depending on the Cre driver used.

Co-culture of bone marrow-derived cDCs with cancer cells recapitulates the tumor-infiltrating actDC state

The scarcity of actDCs within tumors constitutes a major barrier to their functional characterization. Given that actDCs represent a convergent activation state of cDC1s or cDC2s, we asked whether actDCs resembling those infiltrating tumors could be found in conventional FLT3LBMDC cultures (Figure S3A). Using bone marrow from actDC-Sca mice and a standard cDC differentiation protocol (Figure 3A), we observed a distinct Scarlet^{pos} population, particularly within cDC2s (Figure 3B). Addition of live 5555 melanoma cells to fully differentiated FLT3L-BMDCs (Figure 3A) led to a time-dependent increase in Scarlet^{pos} cells within both cDC1 and cDC2 compartments (Figures 3B and S3B). Scarlet^{pos} cells were also observed following exposure to tumor cell-conditioned medium (CM) alone (Figure S3C). Various cancer cell lines drove an increase in Scarlet^{pos} cells to varying degrees (Figure 3C). Scarlet^{pos} cDC1s and cDC2s upregulated MHC-I, MHC-II, CD80, CD86, CD63, PD-L1, PD-L2, and CD40, while IL-12 was selectively upregulated in Scarlet^{pos} cDC1s (Figures 3D–3F), recapitulating the phenotype of tumor-infiltrating actDCs. t-SNE visualization of the analyzed markers revealed that Scarlet expression provided the clearest distinction between actDCs and their resting counterparts (Figure 3D).

To identify tumor-derived signals driving actDC differentiation, we noted that the capacity of different cancer cell lines to induce *in vitro* actDCs correlated with their previously characterized PGE2 production[57] (Figure 3C). Cyclooxygenase-deficient (*Ptgs*$^{-/-}$) tumor cells, unable to produce PGE2,[58] showed reduced actDC-inducing capacity compared with *Ptgs*$^{+/+}$ counterparts, both when using cancer cells directly or CM (Figure S3D). Exogenous PGE2 also increased actDC differentiation in a dose-dependent manner (Figure S3D), identifying tumor-derived PGE2 as one contributing soluble factor *in vitro*. Comparison with poly I:C or lipopolysaccharide (LPS) stimulation showed that whereas tumor cells primarily increased actDC proportions, microbial stimuli additionally enhanced activation marker expression and IL-12 production (Figures S3E–S3G), suggesting that the actDC state can emerge in response to both tumor-derived and microbial cues.

To determine whether *in vitro*-generated actDCs are transcriptionally equivalent to tumor-infiltrating actDCs, we performed single-cell RNA sequencing on CD45^{+} cells from BMDC-cancer cell co-cultures (Figure 3G). This revealed six clusters comprising cDC1s, cDC2s, proliferating cDC1s, proliferating cDC2s, pDCs, and a prominent *Ccr7*-expressing cluster lacking lineage-defining markers that was enriched for an *in vivo* actDC signature (Figures 3G and 3H). These data demonstrated that co-culture with cancer cells generates actDCs that closely resemble tumor-infiltrating actDCs both phenotypically and transcriptionally. To resolve lineage imprints within this convergent actDC cluster, sub-clustering using cDC1/cDC2 module scoring identified two discrete actDC populations aligning with cDC1- and cDC2-associated transcriptional signatures,[36] defined as actDC1s and actDC2s (Figures S3H–S3K). Consistent with this, *in vivo* and *in vitro* actDCs preserved residual protein expression of lineage-defining markers (Figures S1I, S2E, and 3D), indicating that despite converging on a shared CCR7^{+} activation program, actDCs retain lineage-associated features.

CD8^{+} T cell priming against tumor antigens is confined to the actDC state

To functionally characterize actDCs, we added ovalbumin (OVA)-expressing 5555 melanoma cells (5555^{OVA}) to FLT3L-BMDC cultures from actDC-Sca mice and FACS-isolated restDC1s,

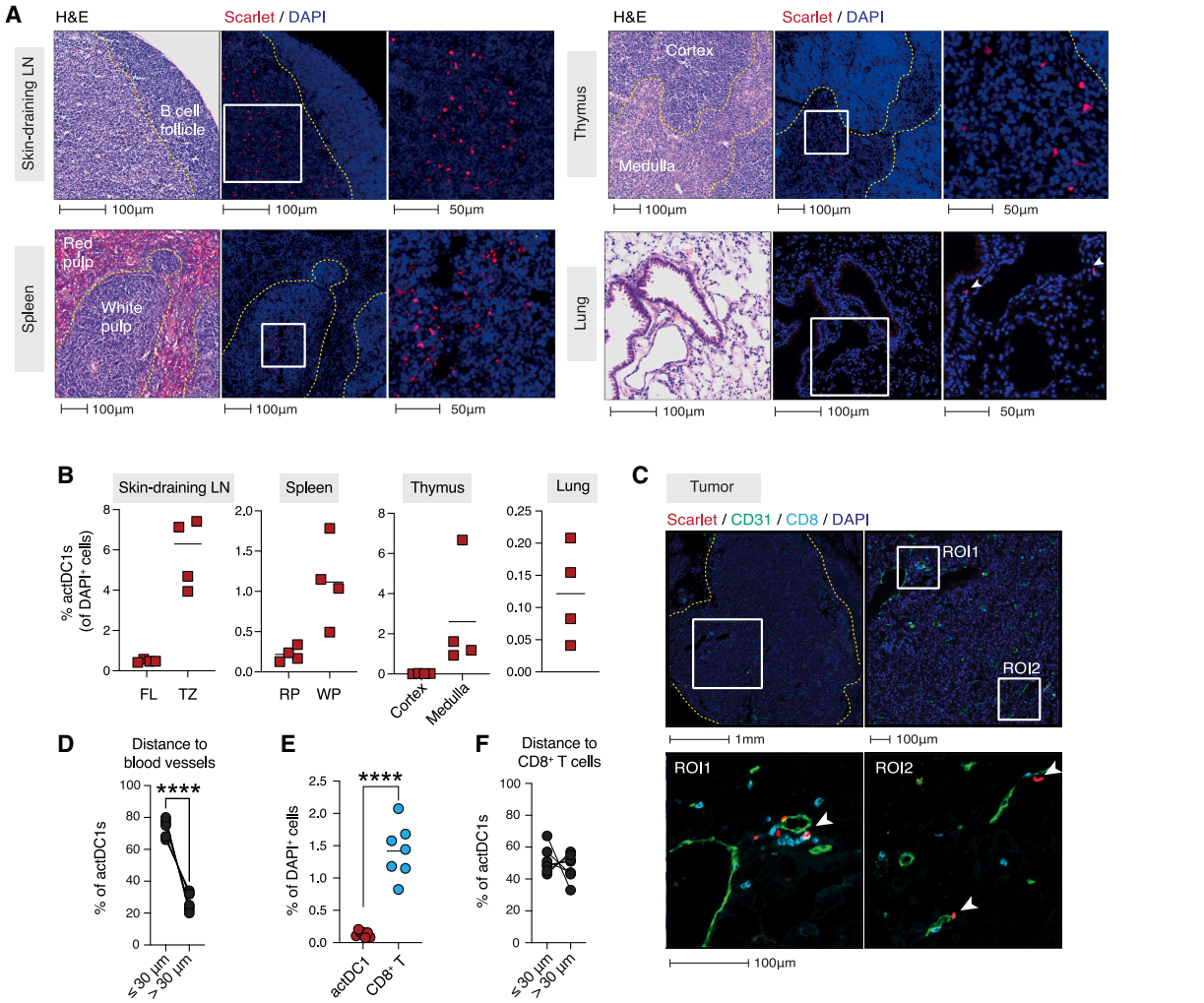

Figure 2. actDC1s localize to distinct microanatomical niches across tissues and tumors

(A) Representative serial H&E and DAPI-stained cryosections of skin-draining LN, spleen, thymus, and lung of actDC1-Sca mice (20× objective). Scale bars: 100 μm (overview) and 50 μm (inset).

(B) Frequency of actDC1s out of total DAPI-stained cells in sections of skin-draining LN, spleen, thymus, and lung of actDC1-Sca mice (n = 4 mice).

(C) Representative fused immunofluorescence images of B16 tumor cryosections stained for CD31 and CD8, at day 7–9 post-implantation. One million cancer cells were injected subcutaneously in the flank of actDC1-Sca mice. Tumor sections were first imaged for Scarlet and then stained with antibodies. Scale bars: 1 mm (overview) and 100 μm (inset).

(D) Frequency of actDC1s within 30 μm distance from blood vessels in B16 tumors (n = 3–4 mice/experiment, pooled from two independent experiments).

(E) Frequency of actDC1s or CD8$^+$ T cells out of total DAPI-stained cells in B16 tumor cryosections of actDC1-Sca mice (n = 3–4 mice/experiment, pooled from two independent experiments).

(F) Frequency of actDC1s within 30 μm distance from CD8$^+$ T cells in B16 tumors (n = 3–4 mice/experiment, pooled from two independent experiments).

Statistical analysis was performed using paired t test (D–F). Statistical significance is indicated as ****$p < 0.0001$. Data are presented as individual values (each dot represents a single mouse), with the mean indicated. FL, B cell follicle; TZ, T cell zone; RP, red pulp; WP, white pulp; ROI, region of interest. Yellow dotted lines delineate anatomical boundaries: FL and TZ in LNs, RP and WP in spleen, medulla and cortex in thymus (A), and margins in subcutaneous tumors (C).

See also Figure S2.

actDC1s, restDC2s, and actDC2s 24 h later to assess their ability to present cancer cell-associated antigens and stimulate proliferation of OVA-specific OT-I cells (Figure 4A). While restDC1s and restDC2s failed to stimulate OT-I proliferation, both actDC1s and actDC2s robustly induced it, unexpectedly to a similar degree (Figure 4A). To confirm this *ex vivo*, we sorted the four DC populations from tumor-dLNs (tdLNs) of actDC-Sca mice bearing 5555^{OVA} tumors (Figure 4B), which are highly immunogenic and spontaneously rejected (Figure S4A), approximately 1 week after cancer cell injection, when tumors reach their maximum size. OT-I proliferation was again exclusively induced by both actDC1s and actDC2s (Figure 4B), indicating that the capacity of cDCs to present cancer cell-associated antigens to CD8$^+$ T cells in the tdLN is confined to the actDC state.

To determine whether the inability of restDCs to prime CD8$^+$ T cells reflected reduced antigen uptake and/or co-stimulation,

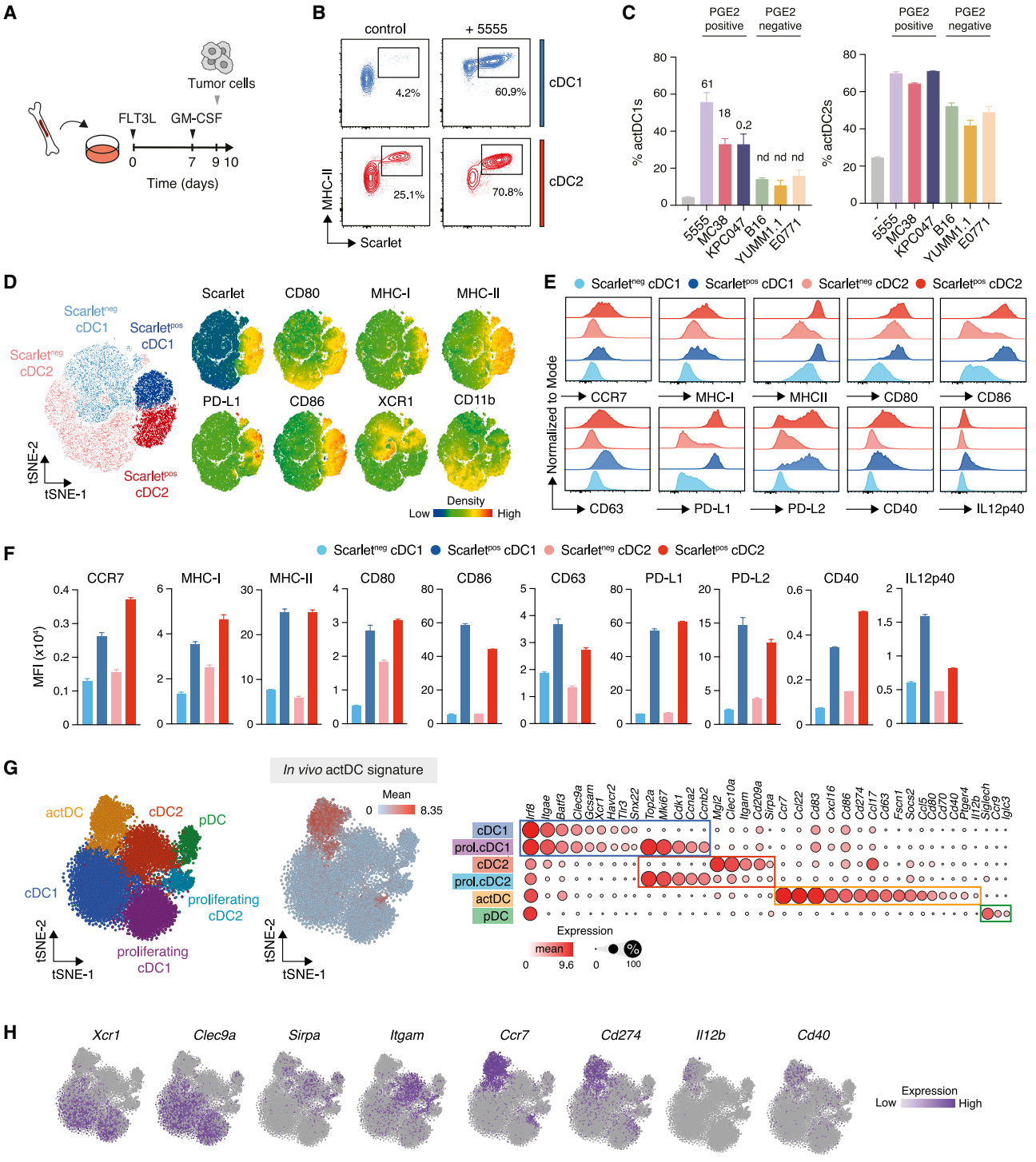

Figure 3. Co-culture with live cancer cells induces the tumor-associated actDC state in BMDC cultures

(A) Schematic of BMDC-cancer cell co-culture setting. Live cancer cells were added directly in FLT3L-BMDC cultures at day 9.

(B) Representative contour plots showing the frequency of Scarlet^{pos} cells in cDC1s or cDC2s in BMDC cultures, in absence or presence of live 5555 cells.

(C) Quantification of the percentage of Scarlet^{pos} cells in cDC1s or cDC2s in BMDC cultures, in presence of melanoma cells (5555, B16, and YUMM1.1), or colorectal (MC38), pancreatic (KPC047), or breast (E0771) cancer cells. Data are presented as mean ± SEM ($n = 2$ technical replicates/group, representative of two independent experiments). Cell lines are ordered according to the level of PGE2 produced by cancer cells *in vitro* (high to low). Concentration of PGE2 in supernatant of cancer cells (ng/mL) is shown on top of each bar (as mean of technical triplicates); nd, not detected.

(legend continued on next page)

we sorted the four *in vitro* cDC populations and incubated them with OT-I cells as described above, now in the presence of the Toll-like receptor (TLR) 9 agonist CpG oligodeoxynucleotide (CpG). Under these conditions, CpG drives DC activation but does not influence prior acquisition of cancer cell-associated antigens. In this setting, all four sorted DC populations promoted OT-I proliferation equally (Figure 4C), supporting the notion that acquisition of cancer cell-associated antigens is not sufficient for $CD8^+$ T cell priming without differentiation into the actDC state.

These results seemed at odds with the notion that the actDC state is induced following antigen and cell debris uptake.[33,34,59,60] Using ZsGreen-expressing 5555 melanoma cells, conventional and imaging flow cytometry showed acquisition and intracellular localization of ZsGreen by all four DC subpopulations, albeit with the highest proportion in actDC1s (Figures 4D, 4E, and S4B). However, both $ZsGreen^{pos}$ and $ZsGreen^{neg}$ DCs transitioned into the actDC state over time in culture and tumor cell CM alone was sufficient to induce actDC differentiation (Figures S3C, S3D, and S4C), indicating that detectable engulfment of cancer cell-derived material is not strictly required for CCR7 upregulation. Consistently, $ZsGreen^{pos}$ and $ZsGreen^{neg}$ restDC1s and restDC2s sorted from BMDC-cancer cell co-cultures showed equal propensity to acquire Scarlet expression (Figure 4F). Although intracellular processing kinetics may limit detection of degraded ZsGreen, these findings indicate that, at least *in vitro*, accumulation of tumor cell-derived material is not a prerequisite for actDC differentiation. Consistent with this, the differential ability of actDCs and restDCs to prime OT-I cells could not be explained by differences in antigen acquisition. Indeed, although similar fractions of actDC2s, restDC1s, and restDC2s acquired cancer cell-derived material (Figures 4D and 4E), only actDC2s drove robust OT-I proliferation.

actDC2s prime $CD8^+$ T cells via cross-dressing

To investigate how actDC2s prime $CD8^+$ T cells, we asked whether cross-dressing, rather than cross-presentation, a hallmark of cDC1s,[13,14,16,17,61] mediates their CTL priming activity. We knocked out β2-microglobulin (β2m) in 5555^{OVA} cells to generate MHC-I-deficient cancer cells unable to cross-dress cDCs (Figures 5A and S5A), implanted them into actDC-Sca mice and sorted DCs from tdLNs for *ex vivo* OT-I co-culture. Only actDC1s induced OT-I proliferation, whereas restDC1s, restDC2s, and actDC2s all failed (Figure 5B), demonstrating that actDC2s rely on cross-dressing, while actDC1s retain the capacity to prime OT-I cells independently of tumor cell MHC-I.

To assess the *in vivo* contribution of cross-dressing to CTL priming, we examined endogenous tumor-specific $CD8^+$ T cell responses in tdLNs of wild-type (WT) mice bearing MHC-I-sufficient or MHC-I-deficient 5555^{OVA} tumors. Consistent with a critical role for CTLs in tumor eradication, MHC-I-sufficient 5555^{OVA} tumors were rejected, whereas MHC-I-deficient tumors grew progressively (Figure S5B). At day 7 after tumor cell implantation, frequencies of H-$2K^b$-SIINFEKL-specific $CD8^+$ T cells and, following SIINFEKL re-stimulation, $IFN\gamma^+$ Granzyme B^+ $CD8^+$ T cells in tdLNs were reduced in mice bearing $B2M^{KO}$ 5555^{OVA} tumors (Figures S5C and S5D), suggesting that cross-dressing contributes to early CTL priming *in vivo*.

To determine whether the contribution of cross-dressing becomes more apparent when cDC1-mediated cross-presentation is limiting, we generated $Irf8^{\Delta 32}$ (cDC1-deficient) (Figure S5E)[62] and $Wdfy4^{-/-}$ (cross-presentation-deficient)[17] mice. In both strains, 5555^{OVA} grew progressively (Figure S5F), consistent with the established requirement for cDC1s and cross-presentation in tumor control.[12,17] We next implanted MHC-I-sufficient or MHC-I-deficient 5555^{OVA} cells into WT, $Irf8^{\Delta 32}$ and $Wdfy4^{-/-}$ mice and transferred naive OT-I cells 3 days later, assessing early activation by CD25 and CD69 upregulation in tdLNs 1 day post-transfer. In WT mice, OT-I activation was comparable regardless of tumor MHC-I status, indicating no detectable cross-dressing contribution when cDC1s and cross-presentation are intact (Figure S5G). In contrast, although OT-I activation was reduced in $Irf8^{\Delta 32}$ and $Wdfy4^{-/-}$ mice, it remained significantly higher in mice bearing MHC-I-sufficient tumors than in those bearing MHC-I-deficient tumors (Figures 5C and 5D). Similarly, endogenous tumor-specific CTL priming in tdLNs was diminished in $Irf8^{\Delta 32}$ and $Wdfy4^{-/-}$ mice when tumor cells lacked MHC-I (Figures S5H and S5I). Collectively, these findings provide evidence that cross-dressing contributes to CTL priming, in particular when cDC1-dependent cross-presentation is limited.

actDC2-mediated $CD8^+$ T cell activation is cancer cell type dependent

Cross-dressing is recognized as a driver of $CD8^+$ T cell-dependent anti-tumor immunity in specific settings,[24,25,63] suggesting that different cancer cell lines might differ in their capacity to cross-dress cDC2s. To test this, we generated OVA-expressing B16 melanoma cells ($B16^{OVA}$) (Figure S5J), co-cultured them with BMDCs and sorted the four DC populations to assess OT-I proliferation (Figure 5E). In contrast to 5555^{OVA} cells (Figures 4A and 4B), only actDC1s stimulated OT-I cells in the $B16^{OVA}$ setting (Figure 5E), indicating that actDC2-mediated CTL priming against tumor-associated antigens depends on properties specific to the cancer cells they encounter.

To investigate the basis of this difference, we noted that despite comparable basal MHC-I levels between 5555^{OVA} and $B16^{OVA}$

(D) t-SNE plots of total cDC1s and cDC2s present in BMDC-cancer cell co-cultures as defined by flow cytometry. Data represent concatenated events from $n = 2$–4 technical replicates/group (2 untreated BMDC wells, 4 BMDC-cancer cell co-cultures and 4 BMDC treated with tumor supernatant). Color-coded overlay of restDC and actDC populations (left), or density plots demonstrating Scarlet expression and surface levels of selected markers (right) are shown.
(E and F) Histograms (E) and quantification (F) of selected surface and intracellular (IL-12p40) markers on restDC1s (light blue), actDC1s (dark blue), restDC2s (pink), and actDC2s (red) from actDC-Sca BMDC-cancer cell co-cultures. These four populations were defined based on the Scarlet signal in cDC1s and cDC2s. Data are presented as mean ± SEM ($n = 2$ technical replicates/experiment, representative of at least two independent experiments).
(G) t-SNE plot generated from single-cell RNA sequencing of sorted $CD45^+$ cells from BMDC cultures in the absence or presence of 5555 melanoma cells. t-SNE plot colored by expression score of the *in vivo* actDC signature (top 20 genes of actDCs infiltrating 5555 melanoma tumors, available in Table S1) and a bubble heatmap showing average levels (color) and frequency (dot size) of marker gene expression across BMDC clusters (pooled data) are shown.
(H) t-SNE plot of BMDCs (pooled data) and expression levels of selected markers.
See also Figure S3.

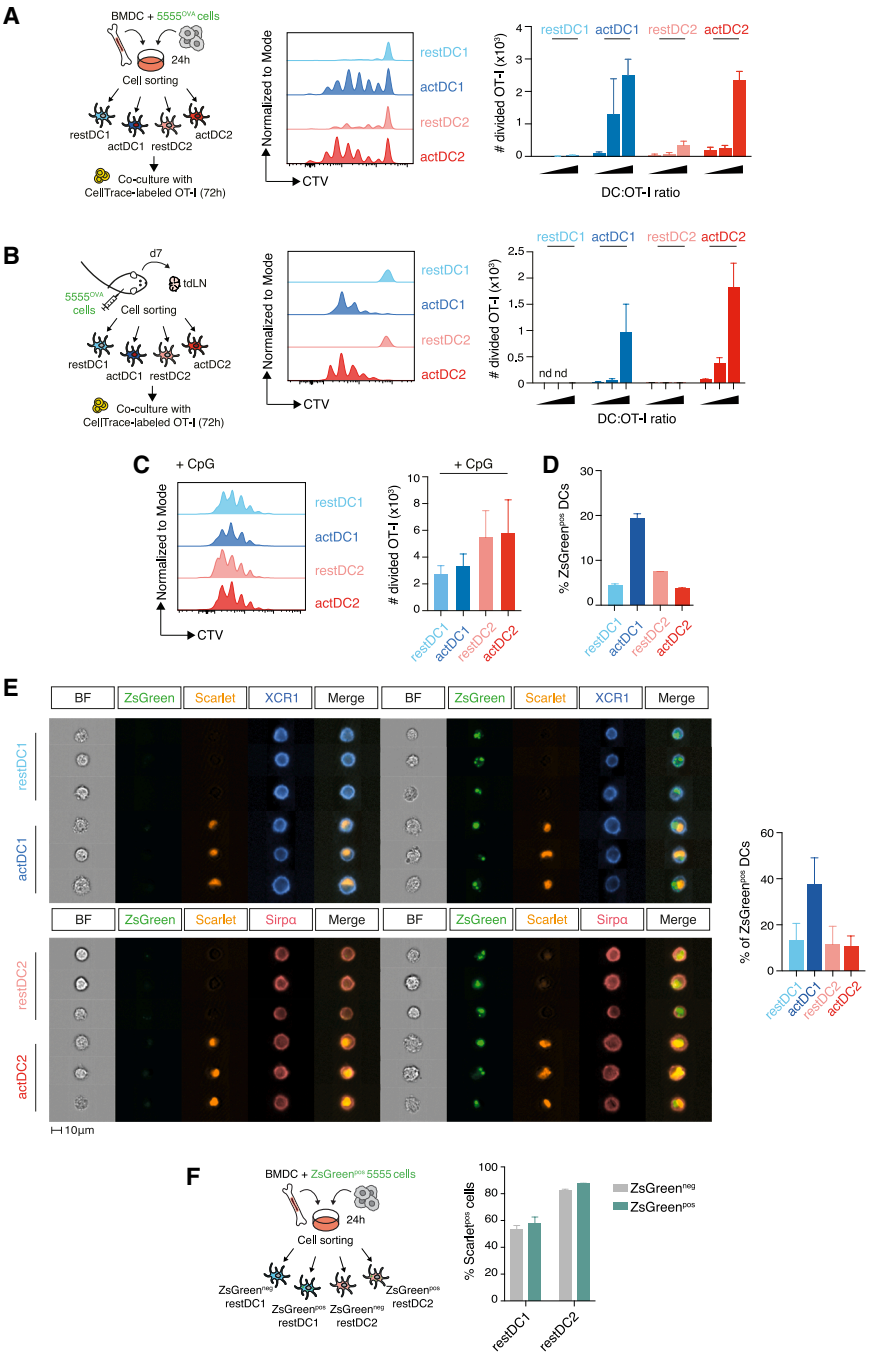

Figure 4. actDC1s and actDC2s, but not restDCs, activate tumor-specific CD8⁺ T cells

(A and B) Schematic of sorting strategy of actDCs and restDCs from BMDCs cultured with OVA-expressing 5555 (5555^{OVA}) cells for 16–24 h (A), or from tdLNs of mice carrying 5555^{OVA} melanoma tumors at day 7 post-implantation (B), and subsequent co-culture with naive, CellTrace Violet (CTV)-labeled OT-I cells. Representative histograms of CTV in OT-I cells and the number of divided OT-I cells after 72 h of co-culture with restDC1s (light blue), actDC1s (blue), restDC2s (pink), and actDC2s (red) are shown; nd, not determined. Data are presented as mean ± SEM (n = 1–3 technical replicates/group). Data are representative of (A), or pooled from (B), at least two independent experiments.

(C) Representative histogram and number of divided OT-I cells after 72 h of co-culture with the specified sorted BMDC populations, in the presence of CpG (added for the DC/OT-I cell co-culture). Data are presented as mean ± SEM (n = 2 technical replicates/group, representative of two independent experiments).

(D) Bar plots showing the accumulation of tumor-derived material in activated or resting cDC populations assessed via standard flow cytometry. Data are presented as mean ± SEM (n = 2 technical replicates/experiment, representative of at least two independent experiments).

(E) Representative images showing engulfment of $ZsGreen^{pos}$ material within restDC1s, actDC1s, restDC2s, and actDC2s, visualized with imaging flow cytometry. Scale bar: 10 μm. Bar plots of the accumulation of tumor-derived material in activated or resting cDC populations assessed via imaging flow cytometry are shown. Data are presented as mean ± SEM (n = 2 biological replicates).

(F) Schematic of sorting strategy of $ZsGreen^{neg}$ and $ZsGreen^{pos}$ restDCs from BMDCs cultured with ZsGreen-expressing 5555 cells for 16 h. Frequency of $Scarlet^{pos}$ cells in sorted populations after overnight culture is shown. Data are presented as mean ± SEM (n = 2–3 technical replicates/group).

See also Figure S4.

cells (Figure S5K), IFNγ pre-treatment of $B16^{OVA}$ cells, which markedly increased surface MHC-I and SIINFEKL-MHC-I complexes (Figure S5K), enabled actDC2s to induce OT-I proliferation comparable to actDC1s (Figures 5F and 5G). To confirm that this reflected enhanced cross-dressing, we generated MHC-I-deficient $B16^{OVA}$ cells, which responded to IFNγ but could not upregulate MHC-I or SIINFEKL-MHC-I complexes (Figures 5H and S5L). In this setting, actDC2s failed to induce OT-I proliferation even following IFNγ pre-treatment (Figure 5I), while actDC1-mediated OT-I activation remained intact and was further enhanced upon co-culture with IFNγ-treated $B2M^{KO}$ $B16^{OVA}$ cells (Figure 5I). Collectively, these data indicate that actDC2-driven CTL priming depends on cross-dressing and that while some cancer cells intrinsically support cross-dressing, others require upregulation of peptide-MHC-I complexes to do so.

The actDC-DTR model enables acute actDC ablation

To evaluate the role of actDCs in anti-tumor immunity *in vivo*, we generated a conditional actDC-depleter strain using the same intersectional strategy as for actDC-Sca, replacing Scarlet with the human diphtheria toxin receptor (DTR) cDNA (Figure 6A). The resulting $Itgax^{Cre}Ccr7^{LSL\text{-}DTR}$ strain, referred to as actDC-DTR, enables inducible ablation of $CCR7^{+}$ DCs upon injection of DT (Figure 6A). As with actDC-Sca, targeting did not affect

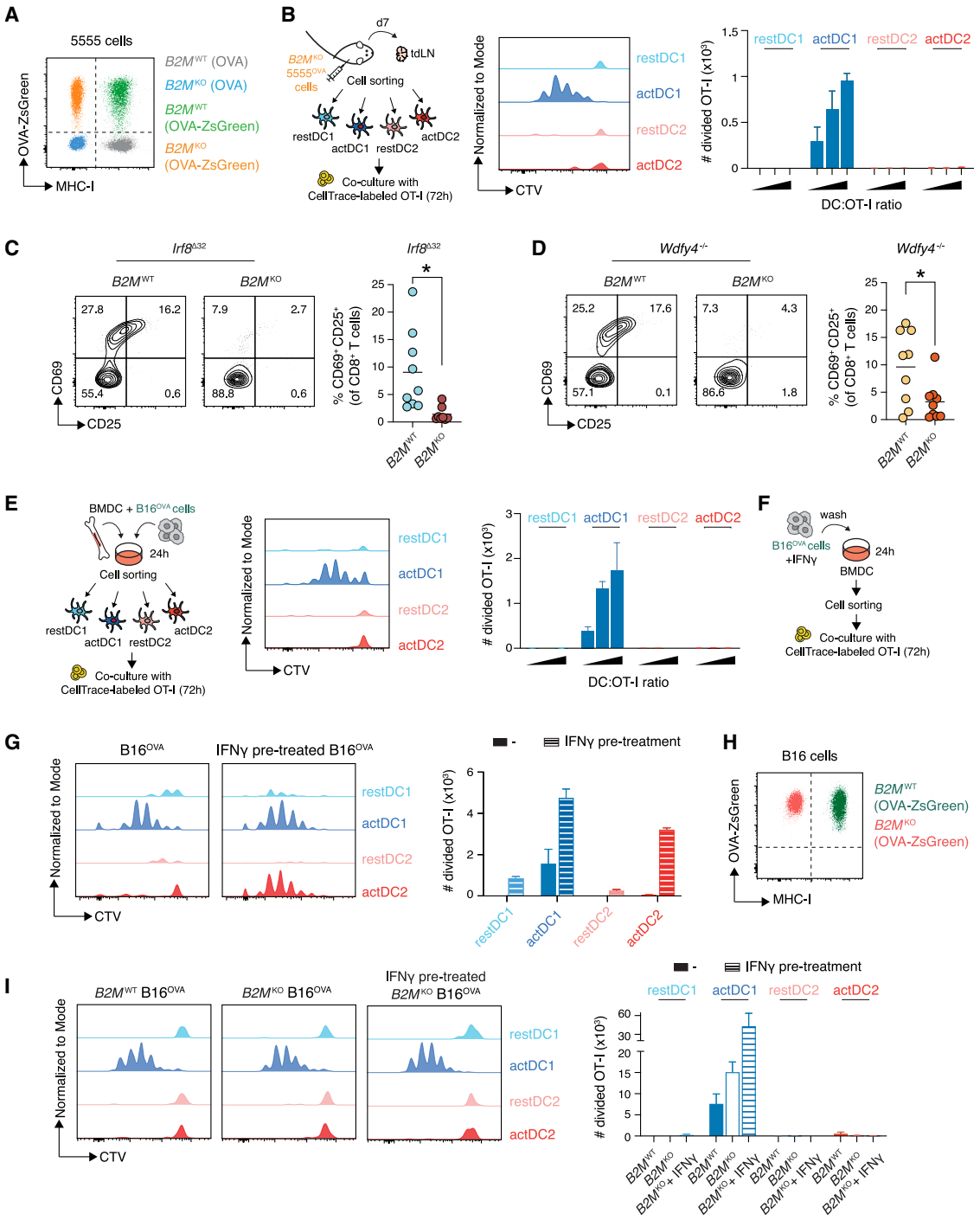

Figure 5. actDC1s cross-present, whereas actDC2s are cross-dressed with, tumor-derived antigen to activate CD8⁺ T cells in a tumor cell type-dependent manner

(A) Representative dot plot showing OVA-ZsGreen and MHC-I levels on the specified 5555 cell lines following overnight treatment with IFNγ.

(B) Schematic of sorting strategy of actDCs and restDCs from tdLNs of mice carrying *B2M*^{KO} 5555^{OVA} melanoma tumors at day 7 post-implantation, and subsequent co-culture with naive, CTV-labeled OT-I cells. Representative histograms and number of divided OT-I cells after 72 h of co-culture with restDC1s, actDC1s, restDC2s, or actDC2s are shown. Data are presented as mean ± SEM (n = 1–3 technical replicates/group, representative of two independent experiments).

(C and D) Representative contour plots and frequency of CD69⁺CD25⁺ OT-I cells present in tdLNs of *Irf8*^{Δ32} (C) or *Wdfy4*$^{-/-}$ (D) mice carrying *B2M*^{WT} or *B2M*^{KO} 5555^{OVA} tumors (n = 8–9 mice/group, pooled from two independent experiments). Data are presented as individual values (each dot represents a single mouse), with the mean indicated. Statistical analysis was performed using unpaired t test. Statistical significance is indicated as $^{*}p < 0.05$.

(legend continued on next page)

CCR7-mediated DC migration (Figure S6A). A single intraperitoneal DT injection led to acute ablation of both actDC1s and actDC2s in the lung within 16–24 h, while restDC1s and restDC2s remained unaffected (Figures 6B, S6B, and S6C). Mice with germline excision of the stop cassette were identified by genotyping and blood phenotyping and excluded (see STAR Methods). Together, these data established actDC-DTR as a suitable model for acute and controllable actDC depletion *in vivo*.

actDCs are essential for spontaneous CTL-mediated rejection of immunogenic tumors

We next used the actDC-DTR strain to evaluate the contribution of actDCs to the T cell response and spontaneous eradication of 5555^{OVA} tumors. Like in WT mice (Figure S4A), 5555^{OVA} tumors spontaneously regressed in PBS-injected actDC-DTR mice but grew progressively in actDC-DTR mice treated with DT (Figure 6C). This was accompanied by a decrease in circulating H-$2K^b$-SIINFEKL-specific $CD8^+$ T cells without affecting the overall $CD8^+$ T cell compartment (Figure 6D), suggesting impaired tumor-reactive T cell priming. Intratumoral analysis confirmed effective ablation of actDC1s and actDC2s with unchanged restDC numbers upon DT (Figures 6E and S6D), and a profound reduction in both $CD8^+$ and $CD4^+$ tumor-infiltrating T cells (Figure 6F). To distinguish direct DT effects on lymphocytes from secondary consequences of actDC depletion, a single DT dose was administered at day 6 post-implantation and immune populations were analyzed 16 h later (Figure S6E). actDC frequencies were significantly decreased in both tumors and tdLNs, whereas restDCs and both $CD4^+$ and $CD8^+$ T cells remained unchanged (Figure S6F), indicating that intratumoral T cell loss is a downstream consequence of sustained actDC depletion rather than direct DT-mediated lymphocyte targeting.

To directly evaluate the role of actDCs in tumor-specific CTL priming, we transferred naive OT-I cells into 5555^{OVA}-bearing actDC-DTR mice and assessed their activation 16 h later (Figure 6G). OT-I cells showed robust CD69 and CD25 upregulation in control actDC-DTR mice but minimal activation following actDC depletion (Figure 6H), demonstrating that early CTL priming depends on the actDC state. $CD4^+$ T cell depletion prior to OT-I transfer did not impair OT-I activation (Figures S6G–S6I), ruling out indirect DT effects mediated by $CD4^+$ T cells. Finally, to begin dissecting the relative contributions of LN and intratumoral actDCs, we inhibited lymphocyte egress using FTY720 in the spontaneously controlled 5555^{OVA} model (Figure S6J). Continuous treatment initiated at tumor implantation abrogated tumor rejection, whereas delayed administration after initial priming allowed transient regression but eventual progression (Figure S6K). Together, these data indicate that durable anti-tumor immunity requires continuous CTL priming and trafficking from LNs to tumors.

The efficacy of ICB and ACT relies on actDCs

Because cDC1s are essential for responses to immunotherapy[3,23,64] beyond T cell priming in tdLNs,[5,10,39] we asked whether actDCs contribute to ICB efficacy. 5555 melanoma cells were implanted into actDC-DTR mice, which were then treated with combined anti-CTLA-4 and anti-PD-1 therapy (Figure 7A). Dual ICB eradicated tumors in control actDC-DTR mice, whereas actDC depletion reduced therapeutic efficacy, with ~40% of mice exhibiting progressive tumor growth (Figures 7B and 7C), indicating that actDCs are critical for responses to ICB. Analysis on day 11 post-implantation, when tumor sizes remained comparable between groups, revealed a significant decrease in both the frequency and absolute number of intratumoral $CD8^+$ T cells, accompanied by decreased numbers of IFNγ-producing $CD8^+$ T cells (Figure S7A) upon actDC depletion. Intratumoral $CD4^+$ T cells also showed a significant decrease in absolute numbers, although their relative frequency was not significantly altered (Figure S7B). The frequencies and numbers of $CD8^+$ and $CD4^+$ T cells in tdLNs and spleen were not significantly decreased at this time point (Figure S7C), supporting the conclusion that actDC depletion impairs anti-tumor T cell responses locally rather than through systemic lymphocyte targeting.

To evaluate the contribution of actDCs to ACT independently of naive T cell priming and rule out potential DT effects on lymphocytes, we crossed actDC-DTR onto a *Rag1*$^{-/-}$ background, thereby eliminating endogenous T and B cells. 5555^{OVA} cells formed aggressive tumors in these mice and a single intravenous infusion of *in vitro*-expanded OT-I cells induced profound but transient tumor shrinkage in all mice (Figures 7D–7F). actDC depletion significantly impaired ACT efficacy (Figures 7E and 7F), with approximately two thirds of mice deriving little or no benefit from therapy, demonstrating that transferred CTL efficacy depends on actDCs. In contrast to the spontaneous tumor control setting (Figures S6J and S6K), ACT efficacy was unaffected by FTY720-mediated blockade of lymphocyte egress (Figures S7D and S7E), consistent with priming being bypassed and supporting a direct role for actDCs at the tumor site. Lastly,

(E) Schematic of sorting strategy of actDCs and restDCs from BMDCs cultured with OVA-ZsGreen-expressing B16 melanoma cells ($B16^{OVA}$) for 16–24 h, and subsequent co-culture with naive, CTV-labeled OT-I cells. Representative histograms of CTV in OT-I cells and the number of divided OT-I cells after 72 h of co-culture with the specified DC population are shown. Data are presented as mean ± SEM (n = 2 technical replicates/group, representative of three independent experiments).

(F) Schematic of sorting strategy of actDCs and restDCs from BMDCs cultured with IFNγ-treated $B16^{OVA}$ cells for 16–24 h, and subsequent co-culture with naive, CTV-labeled OT-I cells.

(G) Representative histograms of CTV in OT-I cells and number of divided OT-I cells after 72 h of co-culture with the specified DC populations. Cancer cells were treated with IFNγ (100 ng/mL) 16–24 h prior co-culture with BMDCs. Data are presented as mean ± SEM (n = 2–3 technical replicates/group, representative of two independent experiments).

(H) Representative dot plot showing OVA-ZsGreen and MHC-I levels on the specified B16 cell lines following overnight treatment with IFNγ.

(I) Representative histograms of CTV in OT-I cells and number of divided OT-I cells after 72 h of co-culture with the specified DC populations. BMDCs were co-cultured for 16–24 h with $B2M^{WT}$ or $B2M^{KO}$ $B16^{OVA}$ cells prior sorting. Cancer cells were treated with IFNγ 16–24 h prior co-culture with BMDCs, as per schematic in (F). Data are presented as mean ± SEM (n = 2–4 technical replicates/group, representative of two independent experiments).

See also Figure S5.

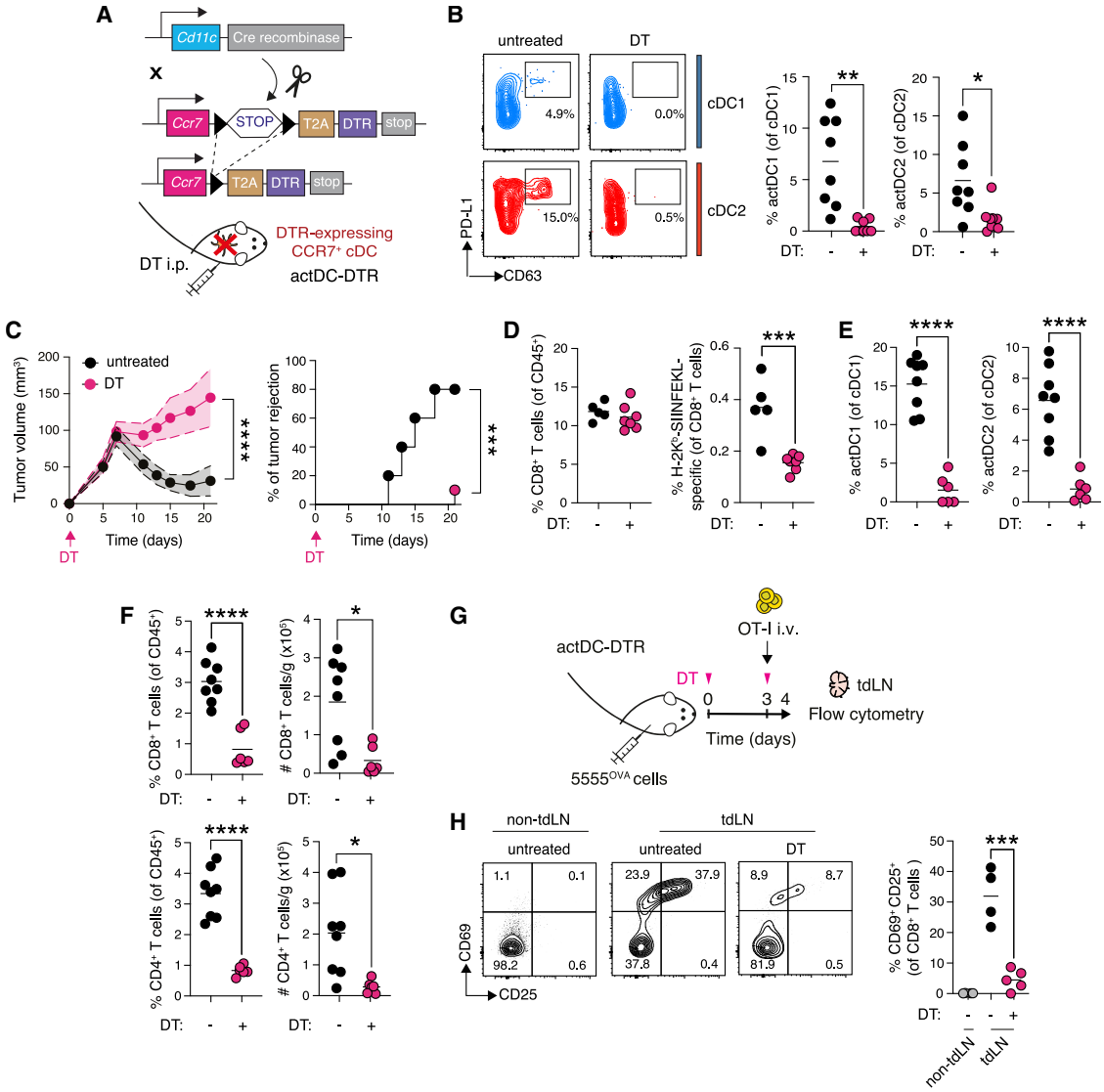

Figure 6. actDCs are required for CD8$^+$ T cell priming and spontaneous tumor regression

(A) Schematic of the design strategy to generate actDC-DTR mice.

(B) Representative contour plots demonstrating actDC gating in cDC1s and cDC2s present in the lung of actDC-DTR mice treated in the absence or presence of DT. The frequency of actDCs in the lung of actDC-DTR mice, treated with or without DT, is shown (n = 8 mice/group, pooled from two independent experiments). Mice were treated with one dose of DT (200 ng/mouse) for 16–24 h.

(C) Growth profile of 5555^{OVA} melanoma tumors on actDC-DTR mice following treatment with PBS or DT (n = 10 mice/group, pooled from two independent experiments). Frequency of rejection of 5555^{OVA} tumors on actDC-DTR mice following treatment with PBS or DT is shown.

(D) Frequency of total or H-2K^b-SIINFEKL-specific CD8$^+$ T cells (defined by pentamer staining) in the blood of actDC-DTR mice treated with PBS or DT, at day 7 post-implantation (n = 5–7 mice/group).

(E) Frequency of actDCs out of total intratumoral cDC1s and cDC2s in actDC-DTR mice carrying 5555^{OVA} tumors (n = 6–8 mice/group, pooled from two independent experiments).

(F) Frequency and numbers of total CD8$^+$ or CD4$^+$ T cells in 5555^{OVA} tumors of actDC-DTR mice (n = 6–8 mice/group, pooled from two independent experiments). DT was administered into actDC-DTR mice intraperitoneally at day 0 (200 ng/mouse), 3 and 6 (100 ng/mouse) post-implantation. Tumor material was analyzed via flow cytometry at day 7 post-implantation.

(G) Schematic of DT and naive OT-I cell administration regimen in actDC-DTR mice injected with 5555^{OVA} cells.

(H) Representative contour plots and frequency of CD69$^+$ CD25$^+$ OT-I cells present in tdLNs of actDC-DTR mice carrying 5555^{OVA} tumors (n = 4–5 mice/group, representative of two independent experiments). Non-tumor-draining LNs (non-tdLNs) were used as a negative control of OT-I activation.

Statistical analysis was performed using two-way ANOVA followed by Šidák's multiple comparison test (C), or unpaired t test (B, D–F, and H). Log-rank (Mantel-Cox) test was performed for "frequency of rejection" curves (C). Statistical significance is indicated as *$p < 0.05$, **$p < 0.01$, ***$p < 0.001$, ****$p < 0.0001$. Data are presented as individual values (each dot represents a single mouse), with the mean indicated.

See also Figure S6.

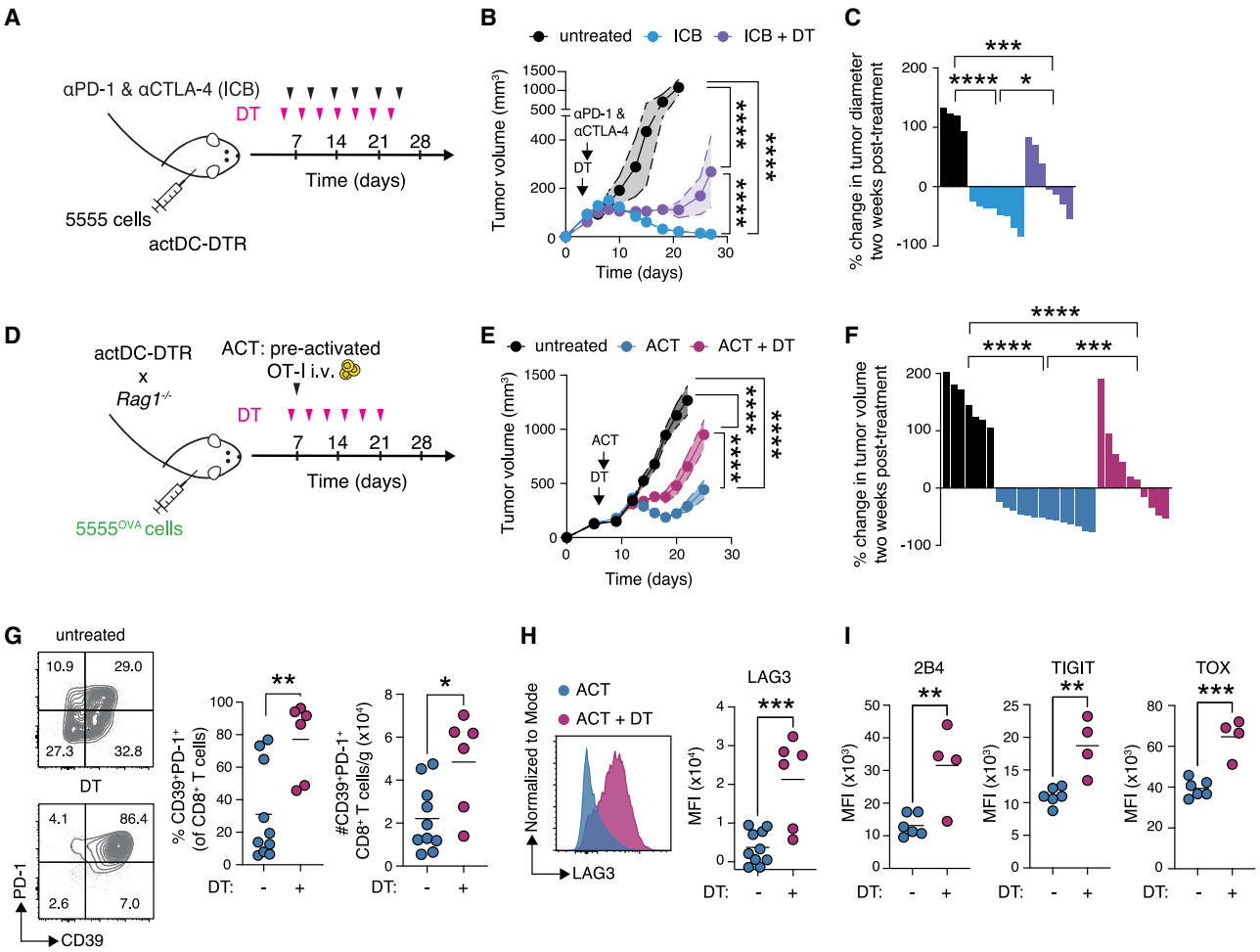

Figure 7. actDC depletion impairs responses to ICB and ACT

(A) Schematic of DT and dual ICB treatment regimen in actDC-DTR mice injected with parental 5555 cells.

(B) Growth profile of 5555 tumors on actDC-DTR mice treated with or without DT and dual ICB (n = 4–8 mice/group, pooled from two independent experiments). Time of treatment initiation is denoted by black arrows on the growth curve.

(C) Waterfall plot showing percentage of change in tumor size after two weeks of dual ICB treatment (n = 4–8 mice/group, pooled from two independent experiments).

(D) Schematic of DT and pre-activated OT-I administration (ACT) regimen in immune-compromised actDC-DTR mice injected with 5555^{OVA} cells.

(E) Growth profile of 5555^{OVA} tumors on immune-compromised actDC-DTR mice treated with or without DT and ACT (n = 7–14/group, pooled from two independent experiments). Time of treatment initiation is denoted by black arrows on the growth curve.

(F) Waterfall plot demonstrating percentage of change in tumor size between day 12 and day 19 post-implantation (n = 7–14/group, pooled from two independent experiments).

(G) Representative contour plots, frequency, and numbers of $CD39^+PD\text{-}1^+$ OT-I cells infiltrating 5555^{OVA} tumors of immune-compromised actDC-DTR mice (n = 6–10/group, pooled from two independent experiments).

(H) Representative histogram and quantification of LAG3 expression on OT-I cells infiltrating 5555^{OVA} tumors of immune-compromised actDC-DTR mice (n = 6–10/group, pooled from two independent experiments).

(I) Representative quantification of 2B4, TIGIT, and TOX expression on OT-I cells infiltrating 5555^{OVA} tumors of immune-compromised actDC-DTR mice (n = 4–6 mice/group).

For flow cytometry experiments, tumors were analyzed at endpoint. Statistical analysis was performed using one-way ANOVA followed by Tukey's multiple comparison test (C and F), two-way ANOVA followed by Šidák's multiple comparison test (B and E) or unpaired t test (G–I). Statistical significance is indicated as $^*p < 0.05$, $^{**}p < 0.01$, $^{***}p < 0.001$, $^{****}p < 0.0001$.

See also Figure S7.

to define how actDCs support ACT efficacy, we examined tumor-infiltrating OT-I cells 2 weeks post-ACT. In actDC-depleted mice, OT-I cells exhibited higher expression of PD-1, CD39, LAG3, 2B4, TIGIT, and TOX compared with actDC-replete controls (Figures 7G–7I and S7F), indicating enhanced T cell dysfunction. Collectively, these data demonstrate that actDCs promote ACT efficacy by restraining terminal dysfunction of transferred tumor-specific $CD8^+$ T cells within tumors.

DISCUSSION

Our current understanding of the function of CCR7$^+$ actDCs in cancer immune responses has been limited due to their scarcity and the lack of experimental tools to unequivocally identify, isolate, or conditionally ablate them. Further complicating their study, markers used to distinguish actDCs from their non-activated restDC counterparts can also be expressed by other immune and non-immune cell populations. In addition, both cDC1s and cDC2s can differentiate into the actDC state while downregulating prototypical markers used to distinguish these two lineages. The selective co-expression by actDCs of T cell-activating (CD80, CD86, and CD40) and inhibitory (PD-L1, PD-L2, and CD200) molecules suggests a dual role in immunity. Together, these features have made it difficult to define the overall contribution of actDCs to anti-tumor immune responses and whether they limit or favor tumor progression.[33,35,39,41,65–67] Here, we described two versatile genetically engineered mouse strains enabling conditional labeling or ablation of CCR7$^+$ actDCs.

Combining the CCR7-Scarlet reporter line with broad DC or cDC1-specific Cre drivers allowed tracking of actDCs or actDC1s, respectively, *in vivo*. These models confirmed that actDCs arise from both cDC1s and cDC2s[27,30,35] and revealed their presence not only across multiple tumor types but also in multiple tissues at steady state. The more restricted actDC1-Sca strain enabled faithful visualization of actDC1s across lymphoid and non-lymphoid tissues and revealed their preferential localization within T cell-rich niches. Within the thymus, actDC1s localized predominantly to the medulla, consistent with a proposed role in central tolerance.[44] Together, these new genetic tools should facilitate defining the contribution of actDCs to immune responses in cancer, infection, and autoimmunity.

The paucity of actDCs in tissues has also hindered their functional characterization. We demonstrated that actDCs phenotypically and transcriptionally equivalent to tumor-infiltrating actDCs can be generated by co-culturing FLT3L-derived BMDCs with cancer cells. The signals driving actDC differentiation across different contexts remain poorly understood. NF-κB signaling, IRF1, uptake of tumor-derived material, the cholesterol biosynthetic pathway, and mechanosensing and phospholipase A2 activity all influence differentiation into the actDC state.[8,20,33,59,60,68] Our findings identify tumor-derived PGE2 as a contributing soluble signal and demonstrate that tumor material engulfment alone is insufficient to induce the actDC state. Accordingly, CCR7$^-$ restDCs bearing tumor antigens failed to promote CD8$^+$ T cell proliferation unless they received additional activation signals, such as TLR agonism. Understanding the barriers to actDC differentiation remains an important area of future work.

CTL priming against cancer cell-associated antigens was confined to the actDC state, with actDC1s and actDC2s being equally effective in the 5555^{OVA} melanoma model. Mechanistically, actDC2s activated CD8$^+$ T cells exclusively through cross-dressing, failing to prime OT-I proliferation when tumor MHC-I was absent. In contrast, actDC1s retained CTL priming capacity independently of tumor MHC-I status, consistent with their unique capacity to cross-present cell-associated antigens. The cancer cell type dependency of actDC2-mediated priming was evident using B16^{OVA} cells, which failed to support it, whereas IFNγ pre-treatment, which markedly increased surface SIINFEKL-MHC-I complexes, restored it. This suggests that the abundance of surface peptide-MHC-I complexes on cancer cells is a critical determinant of cross-dressing. Together with previous evidence that IFN signaling enables cross-dressing,[24] these findings uncover another mechanism by which IFNs contribute to CD8$^+$ T cell-mediated immunity.

Using the actDC-DTR strain, we formally demonstrate that actDCs are essential for spontaneous tumor rejection and for response to ICB. This extends the role of actDCs beyond carrying tumor antigens to tdLNs to prime naive CD8$^+$ T cells.[8] Acute actDC depletion in tumor-bearing lymphocyte-deficient animals significantly limited ACT efficacy following transfer of pre-activated tumor-reactive CTLs, with depleted mice showing accelerated CTL dysfunction within tumors. These data suggest that manipulation of the tumor-infiltrating actDC compartment can enhance ACT responses. Of note, ACT failed to fully eradicate tumors even in the presence of actDCs in lymphocyte-deficient hosts, consistent with a requirement for CD4$^+$ T cells[69] and the formation of triads between cDCs, CD4$^+$ T cells, and CD8$^+$ T cells for sustained ACT efficacy.[70] We speculate that actDCs constitute the DC component of these triads and that CD4$^+$ T cell licensing may fuel the actDC state.[71,72]

actDCs localize within structured immune niches containing CXCL13$^+$ CD4$^+$ T cells and stem-like or effector CD8$^+$ T cells, and the abundance of these niches correlates with responsiveness to ICB across multiple cancer types.[35,37–40,73] CCR7$^+$ actDCs also interact with Tregs, which suppress their migratory capacity and dampen anti-tumor T cell support.[41,56] These studies have largely treated actDCs as a unified population or focused specifically on actDC1s. Our findings that actDC1s and actDC2s exhibit distinct antigen presentation strategies raise the possibility that lineage origin may also determine their spatial positioning and T cell interactions. Future work leveraging the genetic tools described here, combined with refined DC-specific drivers and spatial approaches, should enable dissection of the lineage-resolved spatiotemporal dynamics of actDCs and their contribution to coordinated CD8$^+$ and CD4$^+$ T cell immunity.

In summary, we described new mouse models enabling identification and conditional manipulation of actDCs, providing a versatile platform to explore their biology across disease settings. Using these tools, we demonstrated that the actDC state was essential for natural CTL-mediated anti-tumor immunity as well as for the efficacy of ICB and ACT, positioning actDCs as promising therapeutic targets to improve the efficacy of immunotherapy and other cancer treatments that rely on the cancer-restraining function of the immune system.

Limitations of the study

First, the CD11c-Cre driver used to generate the actDC-Sca and actDC-DTR strains can mediate recombination in CCR7$^+$ lymphocyte populations in which physiological CD11c expression results in excision of the LSL cassette controlling Scarlet or DTR. Although DT treatment did not systematically deplete T or B cells, direct effects on specific CCR7-expressing lymphocytes cannot be excluded, particularly within defined CD8$^+$ T cell subsets preferentially targeted in actDC-Sca mice, and more broadly among tumor antigen-specific T cells. More DC-restricted Cre drivers

will therefore be required in future studies. Second, we focused on the functional role of actDCs rather than the full range of signals driving their differentiation, which likely involves multiple tumor- and host-derived cues. Finally, our analysis was limited to actDCs arising from cDC1 and cDC2 lineages. Similar activation programs may emerge from other lineages, and their developmental origin and state-specific features remain to be defined using our reporter strain combined with multi-omics and lineage-tracing approaches.

RESOURCE AVAILABILITY

Lead contact

Information and requests for resources and reagents should be directed to the lead contact, Santiago Zelenay (santiago.zelenay@cruk.manchester.ac.uk).

Materials availability

Requests for the cancer cell lines and mice generated in this study can be addressed to the lead contact.

Data and code availability

- Single-cell RNA sequencing data have been deposited at the NCBI Gene Expression Omnibus database and can be accessed through the accession number GSE139046 and GSE307145.
- All data and figures will be shared by the lead contact upon request. This paper does not report original code.
- Any additional information required to reanalyze the data reported in this paper is available from the lead contact upon request.

ACKNOWLEDGMENTS

This work was supported by a Cancer Research UK Institute Award (C5759/A27412) to S.Z. E.B. received additional funding from an EMBO advanced fellowship (aALT-638-2108) and the Italian Association for Cancer Research (AIRC), Start-Up grant no. 25828. We thank colleagues in the Cancer Research UK Manchester Institute Core Facilities (Biological Resources Unit, Genome Editing and Mouse Models, Flow Cytometry, Molecular Biology, Computational Biology, Scientific Computing Team, Histology, Visualization, Irradiation and Analysis, Logistics and Lab Services—C5759/A27412) for their support.

AUTHOR CONTRIBUTIONS

M.A.K. conceptualized the study, designed and conducted experiments, analyzed and interpreted data, and wrote the manuscript. E.B. conceptualized the study, designed and conducted experiments, and analyzed and interpreted data. E.R. and V.S.P. designed and conducted experiments. E.R., A.M., S.-C.C., A.B., C.R.B., E.F., M.R., C.H.E., A.P., and P.D. helped perform experiments. E.R., S.-C.C., and L.N.-B. generated CRISPR knockout cell lines. M.A.K., E.B., R.R., V.S.P., and S.S. performed computational analysis. E.R. and E.B. contributed equally to this work. A.S.M., S.H., and B.M. provided oversight and mouse lines. N.M. designed and generated genetically engineered mouse models. S.Z. acquired funding, conceptualized and supervised the study, interpreted data, and wrote the manuscript. All authors reviewed and edited the manuscript.

DECLARATION OF INTERESTS

S.Z. received research grants from Ono Pharmaceutical and Nxera Pharma, and honoraria from Ribonexus, Medibiofarma, iTEOS Therapeutics, Owkin, and Orikine, all unrelated to this work.

STAR★METHODS

Detailed methods are provided in the online version of this paper and include the following:

SUPPLEMENTAL INFORMATION

Supplemental information can be found online at https://doi.org/10.1016/j.immuni.2026.07.002.

Received: July 2, 2025
Revised: March 12, 2026
Accepted: July 5, 2026
Published: August 4, 2026

REFERENCES

1. Thompson, E.D., Enriquez, H.L., Fu, Y.-X., and Engelhard, V.H. (2010). Tumor masses support naive T cell infiltration, activation, and differentiation into effectors. J. Exp. Med. *207*, 1791–1804. https://doi.org/10.1084/jem.20092454.
2. Roberts, E.W., Broz, M.L., Binnewies, M., Headley, M.B., Nelson, A.E., Wolf, D.M., Kaisho, T., Bogunovic, D., Bhardwaj, N., and Krummel, M.F. (2016). Critical Role for CD103(+)/CD141(+) Dendritic Cells Bearing CCR7 for Tumor Antigen Trafficking and Priming of T Cell Immunity in Melanoma. Cancer Cell *30*, 324–336. https://doi.org/10.1016/j.ccell.2016.06.003.
3. Salmon, H., Idoyaga, J., Rahman, A., Leboeuf, M., Remark, R., Jordan, S., Casanova-Acebes, M., Khudoynazarova, M., Agudo, J., Tung, N., et al. (2016). Expansion and activation of CD103+ dendritic cell progenitors at the tumor site enhances tumor responses to therapeutic PD-L1 and BRAF inhibition. Immunity *44*, 924–938. https://doi.org/10.1016/j.immuni.2016.03.012.
4. Wculek, S.K., Cueto, F.J., Mujal, A.M., Melero, I., Krummel, M.F., and Sancho, D. (2020). Dendritic cells in cancer immunology and immunotherapy. Nat. Rev. Immunol. *20*, 7–24. https://doi.org/10.1038/s41577-019-0210-z.
5. Broz, M.L., Binnewies, M., Boldajipour, B., Nelson, A.E., Pollack, J.L., Erle, D.J., Barczak, A., Rosenblum, M.D., Daud, A., Barber, D.L., et al. (2014). Dissecting the tumor myeloid compartment reveals rare activating antigen-presenting cells critical for T cell immunity. Cancer Cell *26*, 638–652. https://doi.org/10.1016/j.ccell.2014.09.007.
6. Garris, C.S., Arlauckas, S.P., Kohler, R.H., Trefny, M.P., Garren, S., Piot, C., Engblom, C., Pfirschke, C., Siwicki, M., Gungabeesoon, J., et al. (2018). Successful Anti-PD-1 Cancer Immunotherapy Requires T Cell-Dendritic Cell Crosstalk Involving the Cytokines IFN-γ and IL-12.

Immunity *49*, 1148–1161.e7. https://doi.org/10.1016/j.immuni.2018.09.024.

7. Mellman, I., Chen, D.S., Powles, T., and Turley, S.J. (2023). The cancer-immunity cycle: Indication, genotype, and immunotype. Immunity *56*, 2188–2205. https://doi.org/10.1016/j.immuni.2023.09.011.
8. Pittet, M.J., Di Pilato, M., Garris, C., and Mempel, T.R. (2023). Dendritic cells as shepherds of T cell immunity in cancer. Immunity *56*, 2218–2230. https://doi.org/10.1016/j.immuni.2023.08.014.
9. Prokhnevska, N., Cardenas, M.A., Valanparambil, R.M., Sobierajska, E., Barwick, B.G., Jansen, C., Reyes Moon, A., Gregorova, P., delBalzo, L., Greenwald, R., et al. (2023). CD8+ T cell activation in cancer comprises an initial activation phase in lymph nodes followed by effector differentiation within the tumor. Immunity *56*, 107–124.e5. https://doi.org/10.1016/j.immuni.2022.12.002.
10. Spranger, S., Dai, D., Horton, B., and Gajewski, T.F. (2017). Tumor-Residing Batf3 Dendritic Cells Are Required for Effector T Cell Trafficking and Adoptive T Cell Therapy. Cancer Cell *31*, 711–723.e4. https://doi.org/10.1016/j.ccell.2017.04.003.
11. Bhandarkar, V., Dinter, T., and Spranger, S. (2025). Architects of immunity: How dendritic cells shape CD8+ T cell fate in cancer. Sci. Immunol. *10*, eadf4726. https://doi.org/10.1126/sciimmunol.adf4726.
12. Hildner, K., Edelson, B.T., Purtha, W.E., Diamond, M., Matsushita, H., Kohyama, M., Calderon, B., Schraml, B.U., Unanue, E.R., Diamond, M.S., et al. (2008). Batf3 deficiency reveals a critical role for CD8alpha+ dendritic cells in cytotoxic T cell immunity. Science *322*, 1097–1100. https://doi.org/10.1126/science.1164206.
13. Bachem, A., Güttler, S., Hartung, E., Ebstein, F., Schaefer, M., Tannert, A., Salama, A., Movassaghi, K., Opitz, C., Mages, H.W., et al. (2010). Superior antigen cross-presentation and XCR1 expression define human CD11c+CD141+ cells as homologues of mouse CD8+ dendritic cells. J. Exp. Med. *207*, 1273–1281. https://doi.org/10.1084/jem.20100348.
14. Crozat, K., Guiton, R., Contreras, V., Feuillet, V., Dutertre, C.-A., Ventre, E., Vu Manh, T.-P., Baranek, T., Storset, A.K., Marvel, J., et al. (2010). The XC chemokine receptor 1 is a conserved selective marker of mammalian cells homologous to mouse CD8alpha+ dendritic cells. J. Exp. Med. *207*, 1283–1292. https://doi.org/10.1084/jem.20100223.
15. Haniffa, M., Shin, A., Bigley, V., McGovern, N., Teo, P., See, P., Wasan, P.S., Wang, X.-N., Malinarich, F., Malleret, B., et al. (2012). Human tissues contain CD141hi cross-presenting dendritic cells with functional homology to mouse CD103+ nonlymphoid dendritic cells. Immunity *37*, 60–73. https://doi.org/10.1016/j.immuni.2012.04.012.
16. Jongbloed, S.L., Kassianos, A.J., McDonald, K.J., Clark, G.J., Ju, X., Angel, C.E., Chen, C.-J.J., Dunbar, P.R., Wadley, R.B., Jeet, V., et al. (2010). Human CD141+ (BDCA-3)+ dendritic cells (DCs) represent a unique myeloid DC subset that cross-presents necrotic cell antigens. J. Exp. Med. *207*, 1247–1260. https://doi.org/10.1084/jem.20092140.
17. Theisen, D.J., Davidson, J.T., Briseño, C.G., Gargaro, M., Lauron, E.J., Wang, Q., Desai, P., Durai, V., Bagadia, P., Brickner, J.R., et al. (2018). WDFY4 is required for cross-presentation in response to viral and tumor antigens. Science *362*, 694–699. https://doi.org/10.1126/science.aat5030.
18. Barry, K.C., Hsu, J., Broz, M.L., Cueto, F.J., Binnewies, M., Combes, A.J., Nelson, A.E., Loo, K., Kumar, R., Rosenblum, M.D., et al. (2018). A natural killer–dendritic cell axis defines checkpoint therapy–responsive tumor microenvironments. Nat. Med. *24*, 1178–1191. https://doi.org/10.1038/s41591-018-0085-8.
19. Böttcher, J.P., Bonavita, E., Chakravarty, P., Blees, H., Cabeza-Cabrerizo, M., Sammicheli, S., Rogers, N.C., Sahai, E., Zelenay, S., and Reis e Sousa, C. (2018). NK Cells Stimulate Recruitment of cDC1 into the Tumor Microenvironment Promoting Cancer Immune Control. Cell *172*, 1022–1037.e14. https://doi.org/10.1016/j.cell.2018.01.004.
20. Ghislat, G., Cheema, A.S., Baudoin, E., Verthuy, C., Ballester, P.J., Crozat, K., Attaf, N., Dong, C., Milpied, P., Malissen, B., et al. (2021). NF-κB-dependent IRF1 activation programs cDC1 dendritic cells to drive antitumor immunity. Sci. Immunol. *6*, eabg3570. https://doi.org/10.1126/sciimmunol.abg3570.
21. Hubert, M., Gobbini, E., Couillault, C., Manh, T.V., Doffin, A.-C., Berthet, J., Rodriguez, C., Ollion, V., Kielbassa, J., Sajous, C., et al. (2020). IFN-III is selectively produced by cDC1 and predicts good clinical outcome in breast cancer. Sci. Immunol. *5*, eaav3942. https://doi.org/10.1126/sciimmunol.aav3942.
22. Michea, P., Noël, F., Zakine, E., Czerwinska, U., Sirven, P., Abouzid, O., Goudot, C., Scholer-Dahirel, A., Vincent-Salomon, A., Reyal, F., et al. (2018). Adjustment of dendritic cells to the breast-cancer microenvironment is subset specific. Nat. Immunol. *19*, 885–897. https://doi.org/10.1038/s41590-018-0145-8.
23. Sánchez-Paulete, A.R., Cueto, F.J., Martínez-López, M., Labiano, S., Morales-Kastresana, A., Rodríguez-Ruiz, M.E., Jure-Kunkel, M., Azpilikueta, A., Aznar, M.A., Quetglas, J.I., et al. (2016). Cancer Immunotherapy with Immunomodulatory Anti-CD137 and Anti-PD-1 Monoclonal Antibodies Requires BATF3-Dependent Dendritic Cells. Cancer Discov. *6*, 71–79. https://doi.org/10.1158/2159-8290.CD-15-0510.
24. Duong, E., Fessenden, T.B., Lutz, E., Dinter, T., Yim, L., Blatt, S., Bhutkar, A., Wittrup, K.D., and Spranger, S. (2022). Type I interferon activates MHC class I-dressed CD11b+ conventional dendritic cells to promote protective anti-tumor CD8+ T cell immunity. Immunity *55*, 308–323.e9. https://doi.org/10.1016/j.immuni.2021.10.020.
25. MacNabb, B.W., Tumuluru, S., Chen, X., Godfrey, J., Kasal, D.N., Yu, J., Jongsma, M.L.M., Spaapen, R.M., Kline, D.E., and Kline, J. (2022). Dendritic cells can prime anti-tumor CD8+ T cell responses through major histocompatibility complex cross-dressing. Immunity *55*, 982–997.e8. https://doi.org/10.1016/j.immuni.2022.04.016.
26. Martinez-Usatorre, A., and De Palma, M. (2022). Dendritic cell cross-dressing and tumor immunity. EMBO Mol. Med. *14*, e16523. https://doi.org/10.15252/emmm.202216523.
27. Cheng, S., Li, Z., Gao, R., Xing, B., Gao, Y., Yang, Y., Qin, S., Zhang, L., Ouyang, H., Du, P., et al. (2021). A pan-cancer single-cell transcriptional atlas of tumor infiltrating myeloid cells. Cell *184*, 792–809.e23. https://doi.org/10.1016/j.cell.2021.01.010.
28. Gerhard, G.M., Bill, R., Messemaker, M., Klein, A.M., and Pittet, M.J. (2021). Tumor-infiltrating dendritic cell states are conserved across solid human cancers. J. Exp. Med. *218*, e20200264. https://doi.org/10.1084/jem.20200264.
29. Qian, J., Olbrecht, S., Boeckx, B., Vos, H., Laoui, D., Etlioglu, E., Wauters, E., Pomella, V., Verbandt, S., Busschaert, P., et al. (2020). A pan-cancer blueprint of the heterogeneous tumor microenvironment revealed by single-cell profiling. Cell Res. *30*, 745–762. https://doi.org/10.1038/s41422-020-0355-0.
30. Zhang, Q., He, Y., Luo, N., Patel, S.J., Han, Y., Gao, R., Modak, M., Carotta, S., Haslinger, C., Kind, D., et al. (2019). Landscape and Dynamics of Single Immune Cells in Hepatocellular Carcinoma. Cell *179*, 829–845.e20. https://doi.org/10.1016/j.cell.2019.10.003.
31. Zilionis, R., Engblom, C., Pfirschke, C., Savova, V., Zemmour, D., Saatcioglu, H.D., Krishnan, I., Maroni, G., Meyerovitz, C.V., Kerwin, C.M., et al. (2019). Single-Cell Transcriptomics of Human and Mouse Lung Cancers Reveals Conserved Myeloid Populations across Individuals and Species. Immunity *50*, 1317–1334.e10. https://doi.org/10.1016/j.immuni.2019.03.009.
32. Ginhoux, F., Guilliams, M., and Merad, M. (2022). Expanding dendritic cell nomenclature in the single-cell era. Nat. Rev. Immunol. *22*, 67–68. https://doi.org/10.1038/s41577-022-00675-7.
33. Maier, B., Leader, A.M., Chen, S.T., Tung, N., Chang, C., LeBerichel, J., Chudnovskiy, A., Maskey, S., Walker, L., Finnigan, J.P., et al. (2020). A conserved dendritic-cell regulatory program limits antitumour immunity. Nature *580*, 257–262. https://doi.org/10.1038/s41586-020-2134-y.
34. Moon, C.Y., Belabed, M., Park, M.D., Mattiuz, R., Puleston, D., and Merad, M. (2025). Dendritic cell maturation in cancer. Nat. Rev. Cancer *25*, 225–248. https://doi.org/10.1038/s41568-024-00787-3.

35. Lee, C.Y.C., Kennedy, B.C., Richoz, N., Dean, I., Tuong, Z.K., Gaspal, F., Li, Z., Willis, C., Hasegawa, T., Whiteside, S.K., et al. (2024). Tumour-retained activated CCR7+ dendritic cells are heterogeneous and regulate local anti-tumour cytolytic activity. Nat. Commun. *15*, 682. https://doi.org/10.1038/s41467-024-44787-1.

36. Cheema, A.S., Duan, K., Dalod, M., and Vu Manh, T.-P. (2023). Harnessing Single-Cell RNA Sequencing to Identify Dendritic Cell Types, Characterize Their Biological States, and Infer Their Activation Trajectory. Methods Mol. Biol. *2618*, 319–373. https://doi.org/10.1007/978-1-0716-2938-3_22.

37. Chen, J.H., Nieman, L.T., Spurrell, M., Jorgji, V., Elmelech, L., Richieri, P., Xu, K.H., Madhu, R., Parikh, M., Zamora, I., et al. (2024). Human lung cancer harbors spatially organized stem-immunity hubs associated with response to immunotherapy. Nat. Immunol. *25*, 644–658. https://doi.org/10.1038/s41590-024-01792-2.

38. Cohen, M., Giladi, A., Barboy, O., Hamon, P., Li, B., Zada, M., Gurevich-Shapiro, A., Beccaria, C.G., David, E., Maier, B.B., et al. (2022). The interaction of CD4+ helper T cells with dendritic cells shapes the tumor microenvironment and immune checkpoint blockade response. Nat. Cancer *3*, 303–317. https://doi.org/10.1038/s43018-022-00338-5.

39. Di Pilato, M., Kfuri-Rubens, R., Pruessmann, J.N., Ozga, A.J., Messemaker, M., Cadilha, B.L., Sivakumar, R., Cianciaruso, C., Warner, R.D., Marangoni, F., et al. (2021). CXCR6 positions cytotoxic T cells to receive critical survival signals in the tumor microenvironment. Cell *184*, 4512–4530.e22. https://doi.org/10.1016/j.cell.2021.07.015.

40. Magen, A., Hamon, P., Fiaschi, N., Soong, B.Y., Park, M.D., Mattiuz, R., Humblin, E., Troncoso, L., D'Souza, D., Dawson, T., et al. (2023). Intratumoral dendritic cell–CD4+ T helper cell niches enable CD8+ T cell differentiation following PD-1 blockade in hepatocellular carcinoma. Nat. Med. *29*, 1389–1399. https://doi.org/10.1038/s41591-023-02345-0.

41. You, S., Li, S., Zeng, L., Song, J., Li, Z., Li, W., Ni, H., Xiao, X., Deng, W., Li, H., et al. (2024). Lymphatic-localized Treg-mregDC crosstalk limits antigen trafficking and restrains anti-tumor immunity. Cancer Cell *42*, 1415–1433.e12. https://doi.org/10.1016/j.ccell.2024.06.014.

42. Remoli, M.E., Ragimbeau, J., Giacomini, E., Gafa, V., Severa, M., Lande, R., Pellegrini, S., and Coccia, E.M. (2007). NF-κB is required for STAT-4 expression during dendritic cell maturation. J. Leukoc. Biol. *81*, 355–363. https://doi.org/10.1189/jlb.0506319.

43. Ye, B.J., Lee, H.H., Yoo, E.J., Lee, C.Y., Lee, J.H., Kang, H.J., Jeong, G.W., Park, H., Lee-Kwon, W., Choi, S.Y., et al. (2020). TonEBP in dendritic cells mediates pro-inflammatory maturation and Th1/Th17 responses. Cell Death Dis. *11*, 421. https://doi.org/10.1038/s41419-020-2632-8.

44. Ardouin, L., Luche, H., Chelbi, R., Carpentier, S., Shawket, A., Montanana Sanchis, F., Santa Maria, C., Grenot, P., Alexandre, Y., Grégoire, C., et al. (2016). Broad and Largely Concordant Molecular Changes Characterize Tolerogenic and Immunogenic Dendritic Cell Maturation in Thymus and Periphery. Immunity *45*, 305–318. https://doi.org/10.1016/j.immuni.2016.07.019.

45. Caton, M.L., Smith-Raska, M.R., and Reizis, B. (2007). Notch–RBP-J signaling controls the homeostasis of CD8- dendritic cells in the spleen. J. Exp. Med. *204*, 1653–1664. https://doi.org/10.1084/jem.20062648.

46. Crozat, K., Tamoutounour, S., Vu Manh, T.-P., Fossum, E., Luche, H., Ardouin, L., Guilliams, M., Azukizawa, H., Bogen, B., Malissen, B., et al. (2011). Cutting edge: expression of XCR1 defines mouse lymphoid-tissue resident and migratory dendritic cells of the CD8α+ type. J. Immunol. *187*, 4411–4415. https://doi.org/10.4049/jimmunol.1101717.

47. Manh, T.-P.V., Alexandre, Y., Baranek, T., Crozat, K., and Dalod, M. (2013). Plasmacytoid, conventional, and monocyte-derived dendritic cells undergo a profound and convergent genetic reprogramming during their maturation. Eur. J. Immunol. *43*, 1706–1715. https://doi.org/10.1002/eji.201243106.

48. Rawat, K., Tewari, A., Li, X., Mara, A.B., King, W.T., Gibbings, S.L., Nnam, C.F., Kolling, F.W., Lambrecht, B.N., and Jakubzick, C.V. (2023). CCL5-producing migratory dendritic cells guide CCR5+ monocytes into the draining lymph nodes. J. Exp. Med. *220*, e20222129. https://doi.org/10.1084/jem.20222129.

49. Abram, C.L., Roberge, G.L., Hu, Y., and Lowell, C.A. (2014). Comparative analysis of the efficiency and specificity of myeloid-Cre deleting strains using ROSA-EYFP reporter mice. J. Immunol. Methods *408*, 89–100. https://doi.org/10.1016/j.jim.2014.05.009.

50. Dalod, M., and Scheu, S. (2022). Dendritic cell functions in vivo: A user's guide to current and next- generation mutant mouse models. Eur. J. Immunol. *52*, 1712–1749. https://doi.org/10.1002/eji.202149513.

51. Wohn, C., Le Guen, V., Voluzan, O., Fiore, F., Henri, S., and Malissen, B. (2020). Absence of MHC class II on cDC1 dendritic cells triggers fatal autoimmunity to a cross-presented self-antigen. Sci. Immunol. *5*, eaba1896. https://doi.org/10.1126/sciimmunol.aba1896.

52. Ferris, S.T., Durai, V., Wu, R., Theisen, D.J., Ward, J.P., Bern, M.D., Davidson, J.T., Bagadia, P., Liu, T., Briseño, C.G., et al. (2020). cDC1 prime and are licensed by CD4+ T cells to induce anti-tumour immunity. Nature *584*, 624–629. https://doi.org/10.1038/s41586-020-2611-3.

53. Mattiuz, R., Wohn, C., Ghilas, S., Ambrosini, M., Alexandre, Y.O., Sanchez, C., Fries, A., Vu Manh, T.-P., Malissen, B., Dalod, M., et al. (2018). Novel Cre-Expressing Mouse Strains Permitting to Selectively Track and Edit Type 1 Conventional Dendritic Cells Facilitate Disentangling Their Complexity in vivo. Front. Immunol. *9*, 2805. https://doi.org/10.3389/fimmu.2018.02805.

54. Calabro, S., Liu, D., Gallman, A., Nascimento, M.S.L., Yu, Z., Zhang, T.T., Chen, P., Zhang, B., Xu, L., Gowthaman, U., et al. (2016). Differential Intrasplenic Migration of Dendritic Cell Subsets Tailors Adaptive Immunity. Cell Rep. *16*, 2472–2485. https://doi.org/10.1016/j.celrep.2016.07.076.

55. Eisenbarth, S.C. (2019). Dendritic cell subsets in T cell programming: location dictates function. Nat. Rev. Immunol. *19*, 89–103. https://doi.org/10.1038/s41577-018-0088-1.

56. Zitti, B., Duval, F., Wirapati, P., Hicham, M., Xie, Y., Oh, J., Hoelzl, J., Meiser, P., Varrone, M., Peterson, H.M., et al. (2026). Positioning and reversible suppression of CCR7+ dendritic cells in perivascular tumor niches shape cancer immunity. Immunity *59*, 161–176.e12. https://doi.org/10.1016/j.immuni.2025.11.020.

57. Bell, C.R., Pelly, V.S., Moeini, A., Chiang, S.-C., Flanagan, E., Bromley, C.P., Clark, C., Earnshaw, C.H., Koufaki, M.A., Bonavita, E., et al. (2022). Chemotherapy-induced COX-2 upregulation by cancer cells defines their inflammatory properties and limits the efficacy of chemoimmunotherapy combinations. Nat. Commun. *13*, 2063. https://doi.org/10.1038/s41467-022-29606-9.

58. Zelenay, S., van der Veen, A.G., Böttcher, J.P., Snelgrove, K.J., Rogers, N., Acton, S.E., Chakravarty, P., Girotti, M.R., Marais, R., Quezada, S.A., et al. (2015). Cyclooxygenase-Dependent Tumor Growth through Evasion of Immunity. Cell *162*, 1257–1270. https://doi.org/10.1016/j.cell.2015.08.015.

59. Belabed, M., Park, M.D., Blouin, C.M., Balan, S., Moon, C.Y., Freed, G., Quijada-Álamo, M., Peros, A., Mattiuz, R., Reid, A.M., et al. (2025). Cholesterol mobilization regulates dendritic cell maturation and the immunogenic response to cancer. Nat. Immunol. *26*, 188–199. https://doi.org/10.1038/s41590-024-02065-8.

60. Bosteels, V., Maréchal, S., De Nolf, C., Rennen, S., Maelfait, J., Tavernier, S.J., Vetters, J., Van De Velde, E., Fayazpour, F., Deswarte, K., et al. (2023). LXR signaling controls homeostatic dendritic cell maturation. Sci. Immunol. *8*, eadd3955. https://doi.org/10.1126/sciimmunol.add3955.

61. Cabeza-Cabrerizo, M., Cardoso, A., Minutti, C.M., Pereira da Costa, M., and Reis e Sousa, C. (2021). Dendritic Cells Revisited. Annu. Rev. Immunol. *39*, 131–166. https://doi.org/10.1146/annurev-immunol-061020-053707.

62. Durai, V., Bagadia, P., Granja, J.M., Satpathy, A.T., Kulkarni, D.H., Davidson, J.T., Wu, R., Patel, S.J., Iwata, A., Liu, T.-T., et al. (2019). Cryptic activation of an Irf8 enhancer governs cDC1 fate specification. Nat. Immunol. *20*, 1161–1173. https://doi.org/10.1038/s41590-019-0450-x.

63. Elewaut, A., Estivill, G., Bayerl, F., Castillon, L., Novatchkova, M., Pottendorfer, E., Hoffmann-Haas, L., Schönlein, M., Nguyen, T.V.,

Lauss, M., et al. (2025). Cancer cells impair monocyte-mediated T cell stimulation to evade immunity. Nature *637*, 716–725. https://doi.org/10.1038/s41586-024-08257-4.

64. Teijeira, A., Garasa, S., Luri-Rey, C., de Andrea, C., Gato, M., Molina, C., Kaisho, T., Cirella, A., Azpilikueta, A., Wculek, S.K., et al. (2022). Depletion of Conventional Type-1 Dendritic Cells in Established Tumors Suppresses Immunotherapy Efficacy. Cancer Res. *82*, 4373–4385. https://doi.org/10.1158/0008-5472.CAN-22-1046.
65. Tang, F., Li, J., Qi, L., Liu, D., Bo, Y., Qin, S., Miao, Y., Yu, K., Hou, W., Li, J., et al. (2023). A pan-cancer single-cell panorama of human natural killer cells. Cell *186*, 4235–4251.e20. https://doi.org/10.1016/j.cell.2023.07.034.
66. Thumkeo, D., Punyawatthananukool, S., Prasongtanakij, S., Matsuura, R., Arima, K., Nie, H., Yamamoto, R., Aoyama, N., Hamaguchi, H., Sugahara, S., et al. (2022). PGE2-EP2/EP4 signaling elicits immunosuppression by driving the mregDC-Treg axis in inflammatory tumor microenvironment. Cell Rep. *39*, 110914. https://doi.org/10.1016/j.celrep.2022.110914.
67. Yang, J., Wang, C., Fu, D., Ho, L.-L., Galani, K., Chen, L., Gonzalez, J., Fu, J., Huang, A.Y., Frederick, D.T., et al. (2025). Mature and migratory dendritic cells promote immune infiltration and response to anti-PD-1 checkpoint blockade in metastatic melanoma. Nat. Commun. *16*, 8151. https://doi.org/10.1038/s41467-025-62878-5.
68. Alraies, Z., Rivera, C.A., Delgado, M.-G., Sanséau, D., Maurin, M., Amadio, R., Maria Piperno, G., Dunsmore, G., Yatim, A., Lacerda Mariano, L., et al. (2024). Cell shape sensing licenses dendritic cells for homeostatic migration to lymph nodes. Nat. Immunol. *25*, 1193–1206. https://doi.org/10.1038/s41590-024-01856-3.
69. Montauti, E., Oh, D.Y., and Fong, L. (2024). CD4+ T cells in antitumor immunity. Trends Cancer *10*, 969–985. https://doi.org/10.1016/j.trecan.2024.07.009.
70. Espinosa-Carrasco, G., Chiu, E., Scrivo, A., Zumbo, P., Dave, A., Betel, D., Kang, S.W., Jang, H.-J., Hellmann, M.D., Burt, B.M., et al. (2024). Intratumoral immune triads are required for immunotherapy-mediated elimination of solid tumors. Cancer Cell *42*, 1202–1216.e8. https://doi.org/10.1016/j.ccell.2024.05.025.
71. Chudnovskiy, A., Castro, T.B.R., Nakandakari-Higa, S., Cui, A., Lin, C.-H., Sade-Feldman, M., Phillips, B.K., Pae, J., Mesin, L., Bortolatto, J., et al. (2024). Proximity-dependent labeling identifies dendritic cells that drive the tumor-specific CD4+ T cell response. Sci. Immunol. *9*, eadq8843. https://doi.org/10.1126/sciimmunol.adq8843.
72. Lei, X., Khatri, I., de Wit, T., de Rink, I., Nieuwland, M., Kerkhoven, R., van Eenennaam, H., Sun, C., Garg, A.D., Borst, J., et al. (2023). CD4+ helper T cells endow cDC1 with cancer-impeding functions in the human tumor micro-environment. Nat. Commun. *14*, 217. https://doi.org/10.1038/s41467-022-35615-5.
73. Piot, C., Pereira da Costa, M., Biram, A., Minutti, C.M., Lim, K.H.J., Green, M., Mikolajczak, A., Jenkins, R.P., Meader, L., Buck, M.D., et al. (2025). Spatial Organisation of Tumour cDC1 States Correlates with Effector and Stem-Like CD8+ T Cells Location. Eur. J. Immunol. *55*, e70011. https://doi.org/10.1002/eji.70011.
74. Bonavita, E., Bromley, C.P., Jonsson, G., Pelly, V.S., Sahoo, S., Walwyn-Brown, K., Mensurado, S., Moeini, A., Flanagan, E., Bell, C.R., et al. (2020). Antagonistic Inflammatory Phenotypes Dictate Tumor Fate and Response to Immune Checkpoint Blockade. Immunity *53*, 1215–1229.e8. https://doi.org/10.1016/j.immuni.2020.10.020.
75. Dhomen, N., Reis-Filho, J.S., da Rocha Dias, S., Hayward, R., Savage, K., Delmas, V., Larue, L., Pritchard, C., and Marais, R. (2009). Oncogenic Braf Induces Melanocyte Senescence and Melanoma in Mice. Cancer Cell *15*, 294–303. https://doi.org/10.1016/j.ccr.2009.02.022.
76. Giampazolias, E., Schulz, O., Lim, K.H.J., Rogers, N.C., Chakravarty, P., Srinivasan, N., Gordon, O., Cardoso, A., Buck, M.D., Poirier, E.Z., et al. (2021). Secreted gelsolin inhibits DNGR-1-dependent cross-presentation and cancer immunity. Cell *184*, 4016–4031.e22. https://doi.org/10.1016/j.cell.2021.05.021.
77. Hao, Y., Stuart, T., Kowalski, M.H., Choudhary, S., Hoffman, P., Hartman, A., Srivastava, A., Molla, G., Madad, S., Fernandez-Granda, C., et al. (2024). Dictionary learning for integrative, multimodal and scalable single-cell analysis. Nat. Biotechnol. *42*, 293–304. https://doi.org/10.1038/s41587-023-01767-y.
78. Weiler, P., Lange, M., Klein, M., Pe'er, D., and Theis, F. (2024). CellRank 2: unified fate mapping in multiview single-cell data. Nat. Methods *21*, 1196–1205. https://doi.org/10.1038/s41592-024-02303-9.
79. Van de Sande, B., Flerin, C., Davie, K., De Waegeneer, M., Hulselmans, G., Aibar, S., Seurinck, R., Saelens, W., Cannoodt, R., Rouchon, Q., et al. (2020). A scalable SCENIC workflow for single-cell gene regulatory network analysis. Nat. Protoc. *15*, 2247–2276. https://doi.org/10.1038/s41596-020-0336-2.
80. Wolf, F.A., Angerer, P., and Theis, F.J. (2018). SCANPY: large-scale single-cell gene expression data analysis. Genome Biol. *19*, 15. https://doi.org/10.1186/s13059-017-1382-0.
81. La Manno, G., Soldatov, R., Zeisel, A., Braun, E., Hochgerner, H., Petukhov, V., Lidschreiber, K., Kastriti, M.E., Lönnerberg, P., Furlan, A., et al. (2018). RNA velocity of single cells. Nature *560*, 494–498. https://doi.org/10.1038/s41586-018-0414-6.
82. Bergen, V., Lange, M., Peidli, S., Wolf, F.A., and Theis, F.J. (2020). Generalizing RNA velocity to transient cell states through dynamical modeling. Nat. Biotechnol. *38*, 1408–1414. https://doi.org/10.1038/s41587-020-0591-3.
83. Spanopoulou, E., Roman, C.A., Corcoran, L.M., Schlissel, M.S., Silver, D.P., Nemazee, D., Nussenzweig, M.C., Shinton, S.A., Hardy, R.R., and Baltimore, D. (1994). Functional immunoglobulin transgenes guide ordered B-cell differentiation in Rag-1-deficient mice. Genes Dev. *8*, 1030–1042. https://doi.org/10.1101/gad.8.9.1030.
84. Hogquist, K.A., Jameson, S.C., Heath, W.R., Howard, J.L., Bevan, M.J., and Carbone, F.R. (1994). T cell receptor antagonist peptides induce positive selection. Cell *76*, 17–27. https://doi.org/10.1016/0092-8674(94)90169-4.
85. Workman, P., Aboagye, E.O., Balkwill, F., Balmain, A., Bruder, G., Chaplin, D.J., Double, J.A., Everitt, J., Farningham, D.A., Glennie, M.J., et al. (2010). Guidelines for the welfare and use of animals in cancer research. Br. J. Cancer *102*, 1555–1577. https://doi.org/10.1038/sj.bjc.6605642.
86. Hodgkins, A., Farne, A., Perera, S., Grego, T., Parry-Smith, D.J., Skarnes, W.C., and Iyer, V. (2015). WGE: a CRISPR database for genome engineering. Bioinformatics *31*, 3078–3080. https://doi.org/10.1093/bioinformatics/btv308.
87. Song, A.J., and Palmiter, R.D. (2018). Detecting and Avoiding Problems When Using the Cre–lox System. Trends Genet. *34*, 333–340. https://doi.org/10.1016/j.tig.2017.12.008.
88. van Blijswijk, J., Schraml, B.U., Rogers, N.C., Whitney, P.G., Zelenay, S., Acton, S.E., and Reis e Sousa, C. (2015). Altered lymph node composition in diphtheria toxin receptor-based mouse models to ablate dendritic cells. J. Immunol. *194*, 307–315. https://doi.org/10.4049/jimmunol.1401999.
89. Aibar, S., González-Blas, C.B., Moerman, T., Huynh-Thu, V.A., Imrichova, H., Hulselmans, G., Rambow, F., Marine, J.-C., Geurts, P., Aerts, J., et al. (2017). SCENIC: Single-cell regulatory network inference and clustering. Nat. Methods *14*, 1083–1086. https://doi.org/10.1038/nmeth.4463.

STAR★METHODS

KEY RESOURCES TABLE

REAGENT or RESOURCE	SOURCE	IDENTIFIER
Antibodies		
anti-mouse CD45-BV605 (clone 30-F11)	BioLegend	Cat# 103140; RRID: AB_2562342
anti-mouse CD45-BV650 (clone 30-F11)	BioLegend	Cat# 103151; RRID: AB_2565884
anti-mouse CD45.2-PE-Cy7 (clone 104)	BioLegend	Cat# 109830; RRID: AB_1186098
anti-mouse CD45.1-APC (clone A20)	BioLegend	Cat# 110713; RRID: AB_313502
anti-mouse B220-eFluor450 (clone RA3-6B2)	eBioscience	Cat# 48-0452-82; RRID: AB_1548761
anti-mouse/human B220-APC (clone RA3-6B2)	BioLegend	Cat# 103212; RRID: AB_312997
anti-mouse/human B220-PE-Cy7 (clone RA3-6B2)	BioLegend	Cat# 103221; RRID: AB_313004
anti-mouse/human B220-PerCP-Cy5.5 (clone RA3-6B2)	BioLegend	Cat# 103235; RRID: AB_893356
anti-mouse CD19-APC (clone eBio1D3)	eBioscience	Cat# 17-0193-80; RRID: AB_1659678
anti-mouse CD19-eFluor450 (clone eBio1D3)	eBioscience	Cat# 48-0193-82; RRID: AB_2734905
anti-mouse CD19-FITC (clone eBio1D3)	eBioscience	Cat# 11-0193-81; RRID: AB_657667
anti-mouse CD19-PE (clone 1D3)	BioLegend	Cat# 152408; RRID: AB_2629817
anti-mouse CD64-PE-Cy7 (clone X54-5/7.1)	BioLegend	Cat# 139314; RRID: AB_2563904
anti-mouse CD64-PE/Dazzle594 (clone X54-5/7.1)	BioLegend	Cat# 139319; RRID: AB_2566558
anti-mouse F4/80-PE-Cy7 (clone BM8)	BioLegend	Cat# 123114; RRID: AB_893478
anti-mouse F4/80-FITC (clone BM8)	BioLegend	Cat# 123108; RRID: AB_893502
anti-mouse Gr-1-BV421 (clone RB6-8C5)	BioLegend	Cat# 108445; RRID: AB_2562903
anti-mouse Gr-1-PE-Cy5 (clone RB6-8C5)	BioLegend	Cat# 108409; RRID: AB_313374
anti-mouse CD63-FITC (clone NVG-2)	BioLegend	Cat# 143919; RRID: AB_2876488
anti-mouse CD63-PE/Dazzle594 (clone NVG-2)	BioLegend	Cat# 143914; RRID: AB_2565504
anti-mouse CD40-PE Cy7 (clone 3/23)	BioLegend	Cat# 124622; RRID: AB_10897812
anti-mouse Ly6C-FITC (clone AL-21)	BD Biosciences	Cat# 553104; RRID: AB_394628
anti-mouse Ly6G-PE/Dazzle594 (clone 1A8)	BioLegend	Cat# 127648; RRID: AB_2566319
anti-mouse Ly6G-AF700 (clone 1A8)	BioLegend	Cat# 127622; RRID: AB_10643269
anti-mouse H-2Kb/H-2Db-APC (clone (28-8-6))	BioLegend	Cat# 114614; RRID: AB_2750194
anti-mouse MHC-II I-A/I-E-APC-eFluor780 (clone M5/114.15.2)	eBioscience	Cat# 47-5321-82; RRID: AB_1548783
anti-mouse MHC-II I-A/I-E-AF700 (clone M5/114.15.2)	eBioscience	Cat# 56-5321-82; RRID: AB_494009
anti-mouse MHC-II I-A/I-E-PerCP-Cy5.5 (clone M5/114.15.2)	BioLegend	Cat# 107626; RRID: AB_2191071
anti-mouse CD11c-PerCP-Cy5.5 (clone N418)	eBioscience	Cat# 45-0114-82; RRID: AB_925727
anti-mouse/human CD11b-BV421 (clone M1/70)	BioLegend	Cat# 101236; RRID: AB_11203704
anti-mouse/human CD11b-BV785 (clone M1/70)	BioLegend	Cat# 101243; RRID: AB_2561373

(*Continued on next page*)

Continued

REAGENT or RESOURCE	SOURCE	IDENTIFIER
anti-mouse/rat XCR1-BV650 (clone ZET)	BioLegend	Cat# 148220; RRID: AB_2566410
anti-mouse/rat XCR1-APC (clone ZET)	BioLegend	Cat# 148206; RRID: AB_2563932
anti-mouse/rat XCR1-FITC (clone ZET)	BioLegend	Cat# 148210; RRID: AB_2564366
anti-mouse/rat XCR1-BV421 (clone ZET)	BioLegend	Cat# 148216; RRID: AB_2565230
anti-mouse CD103-PE (clone 2E7)	eBioscience	Cat# 12-1031-83; RRID: AB_465800
anti-mouse Sirpα-PE-Cy7 (clone P84)	BioLegend	Cat# 144008; RRID: AB_2563546
anti-mouse Sirpα-APC (clone P84)	eBioscience	Cat# 17-1721-82; RRID: AB_10733158
anti-mouse CCR7-AF488 (clone 4B12)	BioLegend	Cat# 120110; RRID: AB_492841
anti-mouse PD-L1-PE (clone MIH5)	eBioscience	Cat# 12-5982-82; RRID: AB_466089
anti-mouse PD-L1-BV421 (clone 10F.9G2)	BioLegend	Cat# 124315; RRID: AB_10897097
anti-mouse PD-L2-BV421 (clone TY25)	BioLegend	Cat# 107219; RRID: AB_2728127
anti-mouse CD3ε-AF488 (clone 145-2C11)	BioLegend	Cat# 100321; RRID: AB_389300
anti-mouse CD3ε-APC (clone 145-2C11)	eBioscience	Cat# 17-0031-82; RRID: AB_469315
anti-mouse CD4-FITC (clone RM4-5)	BioLegend	Cat# 100510; RRID: AB_312713
anti-mouse CD4-AF700 (clone RM4-5)	eBioscience	Cat# 56-0042-82; RRID: AB_494000
anti-mouse CD4-BV650 (clone RM4-5)	BioLegend	Cat# 100555; RRID: AB_2562529
anti-mouse CD8α-PE-Cy7 (clone 53-6.7)	BioLegend	Cat# 100722; RRID: AB_312761
anti-mouse CD8α-PE (clone 53-6.7)	eBioscience	Cat# 12-0081-82; RRID: AB_465530
anti-mouse CD69-FITC (clone H1.2F3)	BioLegend	Cat# 104505; RRID: AB_313108
anti-mouse CD86-BV421 (clone GL-1)	BioLegend	Cat# 105031; RRID: AB_10898329
anti-mouse CD80-FITC (clone 16-10A1)	BioLegend	Cat# 104706; RRID: AB_313127
anti-mouse H-2Kb-SIINFEKL-PE/ Dazzle594 (clone 25-D1.16)	BioLegend	Cat# 141612; RRID: AB_2750522
anti-mouse H-2Kb-SIINFEKL-APC (clone 25-D1.16)	BioLegend	Cat# 141605; RRID: AB_11219402
anti-mouse CD25-PE (clone PC61.5)	eBioscience	Cat# 12-0251-82; RRID: AB_465607
anti-mouse CD62L-APC (clone MEL-14)	BioLegend	Cat# 104412; RRID: AB_313099
anti-mouse PD-1-BV785 (clone 29F.1A12)	BioLegend	Cat# 135225; RRID: AB_2563680
anti-mouse/human TCF-1/7-PE (clone C63D9)	Cell Signaling Technology	Cat# 14456; RRID: AB_2798483
anti-mouse/human CD44-FITC (clone IM7)	eBioscience	Cat# 11-0441-82; RRID: AB_465045
anti-mouse/human CD44-APC-Fire750 (clone IM7)	BioLegend	Cat# 103062; RRID: AB_2616727
anti-mouse NK1.1-APC (clone PK136)	ThermoFisher Scientific	Cat# 17-5941-82; RRID: AB_469479
anti-mouse NK1.1-BV711 (clone PK136)	BioLegend	Cat# 108745; RRID: AB_2563286
anti-mouse LAG3-PerCP-eFluor 710 (clone eBioC9B7W)	eBioscience	Cat# 46-2231-82; RRID: AB_11151334
anti-mouse CD39-PE (clone Duha59)	BioLegend	Cat# 143803; RRID: AB_11219591
anti-mouse/human TOX-APC (clone REA473)	Miltenyi Biotec	Cat# 130-118-474; RRID: AB_2654224
anti-mouse 2B4-FITC (clone eBio244F4)	eBioscience	Cat# 11-2441-82; RRID: AB_657875
anti-mouse TIGIT-BV421 (clone 1G9)	BioLegend	Cat# 142111; RRID: AB_2687311
anti-mouse IL12p40-PE (clone C15.6)	BioLegend	Cat# 505204; RRID: AB_315368
anti-mouse IL12p40-APC (clone C15.6)	BioLegend	Cat# 505206; RRID: AB_315370
anti-human granzyme B-AF700 (clone GB11)	BD Biosciences	Cat# 560213; RRID: AB_1645453
anti-mouse CD16/32 (clone 39)	eBioscience	Cat# 16-0161-85; RRID: AB_468899
anti-mouse IFNγ-eFluor 450 (clone XMG1.2)	eBioscience	Cat# 48-7311-82; RRID: AB_1834366

(*Continued on next page*)

Continued

REAGENT or RESOURCE	SOURCE	IDENTIFIER
anti-mouse TNFα-PE Cy7 (clone MP6-XT22)	eBioscience	Cat# 25-7321-82; RRID: AB_11042728
anti-mouse CD8α (clone EPR21768)	Abcam	Cat# ab217344; RRID: AB_2890649
anti-mouse CD31 (clone MEC13.3)	BioLegend	Cat# 102502; RRID: AB_312909
Donkey anti-rabbit IgG (AF750)	Abcam	Cat# ab175731; RRID: AB_2943056
Donkey anti-rat IgG (AF488)	Invitrogen	Cat# A21208; RRID: AB_2535794
anti-mouse CD4 (clone GK1.5)	Bio X Cell	Cat# BE0003-1; RRID: AB_1107636
anti-mouse CTLA-4 (clone 9D9)	Bio X Cell	Cat# BE0164; RRID: AB_10949609
anti-mouse PD-1 (clone RMP1-14)	Bio X Cell	Cat# BE0146; RRID: AB_10949053
Chemicals, peptides, and recombinant proteins		
Normal Rat Serum	Invitrogen	Cat# 24-5555-94
Brefeldin A Solution (1000X)	eBioscience	Cat# 00-4506-51
Monensin Solution (1000X)	eBioscience	Cat# 00-4505-51
Recombinant mouse IFNγ (PeproTech)	Gibco	Cat# 315-05
Recombinant mouse GM-CSF carrier-free	BioLegend	Cat# 576304
Recombinant mouse FLT3L carrier-free	BioLegend	Cat# 550706
Recombinant mouse CCL21 (6CKine) carrier-free	BioLegend	Cat# 586406
Recombinant mouse IL-2 carrier-free	BioLegend	Cat# 575406
FTY720	Sigma-Aldrich	Cat# SML0700
Cell Stimulation Cocktail (500X)	eBioscience	Cat# 00-4970-03
Red Blood Cell Lysing Buffer Hybri-Max	Sigma-Aldrich	Cat# R7757
ACK Lysing Buffer	Gibco	Cat# A1049201
IC Fixation Buffer	eBioscience	Cat# 00-8222-49
Permeabilization Buffer (10X)	eBioscience	Cat# 00-8333-56
Collagenase IV	Worthington Biochemical	Cat# LS004188
DNase I	Roche	Cat# 11284932001
SIINFEKL OVA257-264	InvivoGen	Cat# vac-sin
Lipofectamine 2000 DNA Transfection Reagent	Invitrogen	Cat# 11668019
Lipofectamine CRISPRMAX	Invitrogen	Cat# CMAX00003
Lipofectamine RNAiMAX	Invitrogen	Cat# 13778-075
Geneticin Selective Antibiotic (G418 sulfate)	Gibco	Cat# 10131027
H2Kb/SIINFEKL pentamer-PE	ProImmune	Cat# F093-2B-G
H2Kb/SIINFEKL tetramer-PE	MHC Tetramer Production Facility, Baylor College of Medicine	N/A
CpG ODN 1668 TLR9 agonist	InvivoGen	Cat# tlrl-1668
Diphtheria Toxin	Sigma-Aldrich	Cat# D0564
Trypan Blue Stain	ThermoFisher Scientific	Cat# T10282
4% PFA in PBS	ThermoFisher Scientific	Cat# J61899
ProLong Gold Antifade Mountant	Invitrogen	Cat# P36930
10 μm latex beads	Beckman Coulter	Cat# 6602796
Critical commercial assays		
6.5mm Transwell with 5.0μm membrane insert	Corning	Cat# 3421
EnGen sgRNA Synthesis kit	New England Biolabs	Cat# E3322
MEGAclear Transcription Clean-Up kit	Life Technologies	Cat# AM1908
NEBuilder HiFi DNA Assembly Cloning kit	New England Biolabs	Cat# E5520
mMESSAGE mMACHINE SP6 Transcription kit	Thermo Fisher Scientific	Cat# AM1340
KOD Hot Start DNA polymerase kit	Sigma-Aldrich	Cat# 71086

(*Continued on next page*)

Continued

REAGENT or RESOURCE	SOURCE	IDENTIFIER
Gibson Assembly Cloning kit	New England Biolabs	Cat# E5510
Naive CD8+ T cell kit	Miltenyi Biotec	Cat# 130-096-543
Prostaglandin E2 Express ELISA kit	Cayman Chemical	Cat# 500141
CellTrace Violet Cell Proliferation kit	ThermoFisher Scientific	Cat# C34571
Foxp3/Transcription Factor Staining Buffer Set kit	eBioscience	Cat# 00-5523-00
LIVE/DEAD Fixable Aqua Dead Cell Stain kit, for 405 nm excitation	Invitrogen	Cat# L34957
Deposited data		
Single-cell RNA sequencing (Sorted CD45$^+$ cells from murine 5555 *Ptgs*$^{-/-}$ tumors)	Bonavita et al.[74]	GSE139046
Single-cell RNA sequencing (Sorted CD45$^+$ cells from murine 5555 *Ptgs*$^{+/+}$ tumors, CT26 tumors, or BMDC cultures)	This study	GSE307145
Experimental models: Cell lines		
Murine 5555 parental (*Ptgs*$^{+/+}$) melanoma cell line	Dhomen et al.[75]	N/A
Murine 5555 COX1/2-deficient (*Ptgs*$^{-/-}$) cell line	Zelenay et al.[58]	N/A
Murine CT26 colorectal carcinoma cell line	Cancer Research UK Manchester Institute	N/A
Murine B16F10 melanoma cell line	Cancer Research UK Manchester Institute	N/A
Murine LA-OVA-ZsGreen 5555 cell line	Cancer Research UK Manchester Institute	This study
Murine LA-OVA 5555 cell line	Cancer Research UK Manchester Institute	This study
Murine ZsGreen 5555 cell line	Cancer Research UK Manchester Institute	This study
Murine LA-OVA-ZsGreen 5555 B2MKO cell line	Cancer Research UK Manchester Institute	This study
Murine LA-OVA 5555 B2M^{KO} cell line	Cancer Research UK Manchester Institute	This study
Murine LA-OVA-ZsGreen B16F10 cell line	Cancer Research UK Manchester Institute	This study
Murine LA-OVA-ZsGreen B16F10 *B2M*^{KO} cell line	Cancer Research UK Manchester Institute	This study
Murine MC38 colorectal carcinoma cell line	Cancer Research UK Manchester Institute	N/A
Murine E0771 mammary cancer cell line	Cancer Research UK Manchester Institute	N/A
Murine YUMM1.1 melanoma cell line	Cancer Research UK Manchester Institute	N/A
Murine KPC047 (TB32047) pancreatic cancer cell line	Albrecht Neese Lab	N/A
Human GP2-293 packaging cell line	Takara Bio	RRID: CVCL_WI48
Experimental models: Organisms/strains		
Mouse: C57BL/6JOlaHsd	Inotiv	Stock No: 057
Mouse: BALB/cOlaHsd	Inotiv	Stock No: 162
Mouse: Hsd:ICR (CD-1)	Inotiv	Stock No: 030
Mouse: *Xcr1*$^{Cre\text{-}mTFP1}$ (*Xcr1*$^{tm2.1(icre)Ciphe}$)	Cancer Research UK Manchester Institute	Wohn et al.[51]
Mouse: *Rag1*$^{-/-}$ (*Rag1*^{tm1Bal})	Cancer Research UK Manchester Institute	N/A
Mouse: *Itgax*^{Cre} (B6.Cg-Tg(*Itgax-cre*)1-1Reiz/J)	Cancer Research UK Manchester Institute	N/A
Mouse: CD45.1 OT-I *Rag1*$^{-/-}$ (Tg(TcraTcrb)1100Mjb/J;*Rag1*^{tm1Bal})	Cancer Research UK Manchester Institute	N/A
Mouse: *Ccr7*$^{LSL\text{-}mScarlet\text{-}I}$ (*Ccr7*$^{em1(LSL\text{-}mScarlet)Szel}$)	Cancer Research UK Manchester Institute	This study
Mouse: *Ccr7*$^{LSL\text{-}DTR}$ (*Ccr7*$^{em2(LSL\text{-}Hbegf)Szel}$)	Cancer Research UK Manchester Institute	This study
Mouse: *Wdfy4*$^{-/-}$ (*Wdfy4*^{em1Szel})	Cancer Research UK Manchester Institute	This study
Mouse: *Irf8*$^{\Delta 32}$ (*Irf8*^{em1Szel})	Cancer Research UK Manchester Institute	This study

(*Continued on next page*)

Continued		
REAGENT or RESOURCE	SOURCE	IDENTIFIER
Oligonucleotides		
Please refer to Table S2	N/A	N/A
Recombinant DNA		
Plasmid: pHIV-ZsGreen	Addgene	RRID: Addgene_18121
Plasmid: pMSCV-IRES-Life-Act-OVA-mCherry	Giampazolias et al.[76]	N/A
Plasmid: pFB-neo retroviral vector	Agilent Technologies	Cat# 217561
Plasmid: pCS2+-Cas9-mSA	Addgene	RRID: Addgene_103882
Software and algorithms		
FlowJo v10.10.1	FlowJo, LCC	RRID: SCR_008520
Partek Flow software (Single cell Toolkit) build version 12.3.0	Partek	https://help.partek.illumina.com/
GraphPad Prism v10.2.3	GraphPad Software	RRID: SCR_002798
HALO v4.0.5107.407	Indica Labs	RRID: SCR_018350
IDEAS v6.2	Amnis	https://cytekbio.com/pages/imagestream
Python v3.10.12	Python Software Foundation	https://www.python.org/ RRID:SCR_008394
Seurat v.5.3.1	Rahul Satija Lab	Hao et al.[77] RRID: SCR_016341
R software	R Project for Statistical Computing	https://www.r-project.org/ RRID:SCR_001905
Cell Ranger v3.0.2	10x Genomics	https://www.10xgenomics.com
CellRank	Fabian J. Theis Lab	Weiler et al.[78] RRID:SCR_022827
PySCENIC v0.12.1	Stein Aerts Lab	Van de Sande et al.[79]
Scanpy	Fabian J. Theis Lab	Wolf et al.[80] RRID: SCR_018139
Velocyto v0.17.25	Peter V. Kharchenko Lab	La Manno et al.[81]
scVelo v0.3.2	Fabian J. Theis Lab	Bergen et al.[82] RRID:SCR_018168

EXPERIMENTAL MODEL AND STUDY PARTICIPANT DETAILS

Mice

All mice were housed in individually ventilated cages at the Cancer Research UK Manchester Institute animal facility under specific pathogen-free conditions in a 12h light/dark cycle, with irradiated food and autoclaved water available *ad libitum*. Wild-type mice used were on a C57BL/6JOlaHsd or BALB/c background (ENVIGO). The genetically modified strains *Rag1*$^{-/-}$ (*Rag1*^{tm1Bal}),[83] *Itgax*^{Cre} (B6.Cg-Tg(*Itgax-cre*)1-1Reiz/J),[45] *Xcr1*$^{Cre\text{-}mTFP1}$ (*Xcr1*$^{tm2.1(icre)Ciphe}$)[51] and CD45.1 OT-I *Rag1*$^{-/-}$ (Tg(TcraTcrb)1100Mjb/J;*Rag1*^{tm1Bal})[84] in a C57BL/6JOlaHsd background were bred and maintained at Cancer Research UK Manchester Institute. Both female and male mice were used in procedures at 6-12 weeks of age. Mice were sex- and age-matched for use in experiments. The overall program of work relating to these experiments was approved by the Animal Welfare and Ethical Review Body (AWERB) of the Cancer Research UK Manchester Institute during the project license application (license PDCC31AAF and PP4470150). *In vivo* experiments were reported in line with ARRIVE guidelines and National Home Office regulations under the Animals (Scientific Procedures) Act 1986. Maximum tumor volume did not exceed 1500 mm^3, according to the guidelines set by the Committee of the National Cancer Research Institute,[85] as recommended by the AWERB.

Cell lines

The CT26, MC38, E0771, B16, YUMM1.1 as well as the GP2-293 cell line are commercially available. The KPC047 (TB32047) cell line was kindly provided by Albrecht Neese lab. The Braf^{V600E}-driven 5555 melanoma cell line was established from C57BL/6 *Braf*$^{+/LSLV600E}$*Tyr::CreERT2*$^{+/o}$*p16*$^{INK4a-/-}$ mice.[75] Ptgs$^{-/-}$ 5555 cells were generated by CRISPR/Cas9-mediated genome engineering as previously described.[58] Cancer cell lines were grown at 5% CO_2, 37°C and 95% humidified cell culture incubator and cultured in RPMI (Lonza) supplemented with 10% heat-inactivated fetal bovine serum (FBS – Life Technologies) and 1% penicillin/streptomycin (ThermoFisher Scientific) (referred as complete RPMI). All cancer cell lines used in experiments had a low passage number and were routinely tested for mycoplasma contamination (Venor® GeM gEP Mycoplasma Detection Kit, Minerva Biolabs) and mouse hepatitis virus (QIAamp® Viral RNA Mini extraction kit, Qiagen) by qPCR. For tumor cell CM preparation, supernatant from flasks containing

5555 melanoma cells with 80-90% confluency was collected and centrifuged at 1300rpm for 5min to remove cellular debris. Supernatant was then passed through a 0.45 μm syringe filter, aliquoted and stored at -20°C. Concentration of PGE2 in cell supernatants was monitored by ELISA (Cayman Chemical).

Bone marrow-derived DC culture

To generate cDCs for *in vitro* experiments, bone marrow was isolated from tibiae and femurs of naive mice that were humanely euthanized by cervical dislocation (Schedule 1, Animals [Scientific Procedures] Act 1986). Bone marrow was filtered through a 70 μm cell strainer. Red blood cells (RBCs) were removed using an RBC lysis buffer (Sigma-Aldrich) and primary bone marrow cells were cultured in complete RPMI supplemented with 0.1% 2-mercaptoethanol (DC medium) and FLT3L (150 ng/mL, BioLegend) on a 6-well plate. GM-CSF (20 ng/mL, BioLegend) was added in the primary BMDC cultures on day 7. On day 9 or 10, non-adherent cells were harvested by gentle pipetting, counted using a Countess automated cell counter (ThermoFisher Scientific) and used for subsequent *in vitro* cell assays. Dendritic cells were ≥90% viable after harvesting, as determined by Trypan Blue (ThermoFisher Scientific) exclusion.

METHOD DETAILS

Generation of *Ccr7*$^{LSL\text{-}mScarlet\text{-}I}$ and *Ccr7*$^{LSL\text{-}DTR}$ mice

Ccr7$^{LSL\text{-}mScarlet\text{-}I}$ (C57BL/6JOlaHsd-*Ccr7*$^{em1(LSL\text{-}mScarlet)Szel}$) and *Ccr7*$^{LSL\text{-}DTR}$ (C57BL/6JOlaHsd-*Ccr7*$^{em2(LSL\text{-}Hbegf)Szel}$) mice were generated using a CRISPR-Cas9 approach by introducing immediately upstream of the stop codon, an LSL cassette followed by Scarlet (tagged with histone 2B or H2B) and DTR, respectively (related to Figures 1D and 6A). Briefly, using the Wellcome Sanger Institute Genome Editing online tool (https://wge.stemcell.sanger.ac.uk),[86] sgRNAs (5'-CCCCTACGGGGAGAAGGTTGTGG and 5'-GGGCAGGGGAGCCCCCTACGGGG) were designed targeting the region of interest. sgRNAs were synthetized using EnGen sgRNA Synthesis kit (New England Biolabs) and purified with MEGAclear Kit (Thermo Fisher Scientific). To construct the repair templates, H2B-Scarlet-TKstop and DTR/Hbegf-TKstop gBlock fragments (Integrated DNA technologies) were individually cloned into pBlueScript II SK(+). A loxP-flanked stop cassette, followed by a T2A self-cleavage peptide sequence and both homology arms (amplified from gDNA) were then cloned into each pBS.H2B.Scarlet.TK and pBS.DTR.TK plasmid. All cloning steps were done using NEBuilder HiFi DNA Assembly Cloning Kit (New England Biolabs). DNA fragments spanning homology arms and knock-in inserts were PCR-amplified from the plasmids with T3 and T7 primers with 5'-biotin modification. PCR products were subsequently purified to generate biotinylated PCR donors for zygote microinjection. To produce Cas9 fused to monomeric streptavidin (Cas9-mSA) mRNA, pCS2+-Cas9-mSA plasmid (Addgene #103882) was linearized with NotI restriction enzyme and used as template for *in vitro* transcription with a mMESSAGE mMACHINE SP6 Transcription Kit (Thermo Fisher Scientific). The resulting mRNA was then purified using MEGAclear Kit (Thermo Fisher Scientific).

Four-week-old female C57BL/6JOlaHsd mice were superovulated using HyperOva (CosmoBio USA) and hCG and mated to C57BL/6JOlaHsd stud males. Fertilized embryos were collected from oviducts. Mice were generated by cytoplasmic microinjection of Cas9-mSA mRNA (70 ng/μl), sgRNAs (50 ng/μl each) and biotinylated PCRs (20 ng/μl) into zygotes. Microinjected embryos were cultured overnight in EmbryoMax Advanced KSOM Embryo Medium (KSOM, Sigma-Aldrich) and surgically implanted into the oviduct of Hsd:ICR (CD-1®) pseudopregnant mice 0.5 days post coitum. Offspring were screened for correct targeting using PCR primers flanking both 5' and 3' homology arms, followed by Sanger sequencing. Correct targeting was confirmed for one founder for each new mouse line using the same genotyping approach. Established colonies were genotyped by Transnetyx using real-time PCR with specific probes for Cre targeting and the different alleles: wild-type, Cre-conditional (''floxed'') and targeted (''recombined'') allele, to assess potential unexpected recombination (for instance detecting animals with germline recombination that are Cre-negative but excised allele-positive). In addition to rigorous genotyping, we implemented a breeding strategy in which only the sire carried the Cre transgene, in order to reduce the risk of unwanted recombination.[87] This was further controlled by monitoring T and B cell numbers in the blood of actDC-DTR mice after DT injection, where mice with germline Cre expression can be identified by their drastic and abrupt reduction in T and B cells.

As previously reported for DC-targeted DTR models, actDC-DTR mice displayed baseline LN hypocellularity,[88] highlighting the necessity of using actDC-DTR mice with or without DT as matched experimental controls. To minimize DT-associated toxicity, experiments were performed in 11-12-week-old actDC-DTR mice.

Generation of *Wdfy4*$^{-/-}$ and *Irf8*$^{\Delta 32}$ mice

New *Wdfy4*$^{-/-}$ (C57BL/6JOlaHsd-*Wdfy4*^{em1Szel}) and *Irf8*$^{\Delta 32}$ (C57BL/6JOlaHsd-*Irf8*^{em1Szel}) mouse lines were generated using a CRISPR-Cas9 genome editing approach. Using the online tool mentioned above, two sgRNAs were designed for *Wdfy4* flanking exon 4 (5'-GTTTTGGGAGCTGCGTGGATAGG and 5'-CAGGCCTCGAAGGTGTTCCCAGG; Integrated DNA Technologies). A similar strategy was employed to target the *Irf8* +32 enhancer region, using sgRNAs 5'-GTTGTGATCTTTGAGGTAGAGGG and 5'-GAACTGGCCTGGGGCAGGTCTGG (Integrated DNA Technologies).

Superovulation of four-week-old female C57BL/6JOlaHsd mice was induced as described above. Oocytes were collected and used for *in vitro* fertilization with sperm from C57BL/6JOlaHsd male. Zygotes were electroporated with ribonucleotide protein complexes containing sgRNAs (100 ng/μl) and Cas9 HiFiCas9 v3 (500 ng/μl; Integrated DNA Technologies) in Opti-MEM media (Thermo Fisher Scientific) using Nepa21 electroporator (Nepagene). Following electroporation, zygotes were cultured overnight in KSOM

(Sigma-Aldrich) media and two-cell embryos were surgically implanted into the oviduct of Hsd:ICR (CD-1) pseudopregnant mice 0.5 days post coitum. Offspring were assessed for the intended deletions using primers flanking the targeted regions (Table S2), followed by Sanger sequencing.

Plasmid construction and retroviral transduction

For generating OVA- and ZsGreen-expressing cancer cell lines, PCR products (amplified using the KOD Hot Start DNA polymerase kit, Sigma-Aldrich) of the fused LifeAct F-actin binding peptide-OVA (LA-OVA) fragment from pMSCV-IRES-Life-Act-OVA-mCherry[76] or/and ZsGreen from pHIV-ZsGreen (Addgene, #18121) were combined with the pFB-neo retroviral expression vector (Agilent Technologies) using the Gibson Assembly ® Cloning kit (New England Biolabs). The primers used for each construct are available in Table S2. Resulting constructs were verified through Sanger sequencing. GP2-293 cells (Takara Bio) were infected with the desired retroviral packaging plasmid pFBneo containing gene/insert of interest a 1:1 molar ratio with the envelope plasmid pVSV-G, using the Lipofectamine 2000 DNA Transfection Reagent (Invitrogen). Supernatant containing viral particles was collected 48h after transfection. For cancer cell transduction, viral supernatant containing 5 μg/mL polybrene was added to parental 5555 or B16 melanoma cultures. Infection was enhanced through centrifugation at 2500 rpm for 90min at 32°C. After 24h, infected cells were cultured in the presence of 800 μg/mL G418 selection antibiotic (Gibco) for 72h and transduction efficiency was assessed through cell death confirmation in the untransduced negative control. ZsGreen expression was validated by flow cytometry as well as imaging using the IncuCyte S3 instrument (Sartorius). Following overnight treatment with recombinant IFNγ (100 ng/mL, Gibco), LA-OVA expression was confirmed by flow cytometry using an H-2K^{b}-SIINFEKL (25-D1.16) antibody. Cancer cells with stable expression of ZsGreen and/or LA-OVA were always grown in selection medium for one to two passages prior injection into mice.

Generation of CRISPR knockout cell lines

5555 and B16 *B2M*^{KO} melanoma cells were generated by CRISPR-Cas9-mediated gene editing using the ribonucleoprotein (RNP) approach (Integrated DNA Technologies), following manufacturer's protocol. For the RNP complex assembly, 1.5pmol Cas9 enzyme was combined with 1.5pmol crRNA:trRNA duplex (Table S2) in Opti-MEM media (Gibco) and incubated at room temperature for 5 min. The RNP complex was then combined with Lipofectamine CRISPRMAX or RNAiMAX (Invitrogen) and Opti-MEM and incubated at room temperature for 20 min. 5555 or B16 cells were trypsinized, washed with PBS and 4x10^{4} (for 5555) or 1x10^{4} (for B16) cells were added to the transfection mixture in a 96-well plate. At 48h post-transfection, single cell suspensions were re-plated in 96-well plates at a concentration of 3 cells/mL to develop into macroscopic colonies. Colony screening for MHC-I knockout was performed following overnight treatment with recombinant IFNγ (100 ng/mL, Gibco) by flow cytometry using an H-2K^{b}/H-2D^{b} antibody (28-8-6).

In vivo procedures

For subcutaneous injections, cancer cells grown at exponential phase were trypsinized (Sigma-Aldrich), washed three times in ice-cold DPBS (ThermoFisher Scientific) and filtered through a 70 μm cell strainer (ThermoFisher Scientific). Cancer cell viability ≥90% was confirmed through Trypan Blue stain prior injection. 1-2x10^{6} cells were suspended in 100 μL DPBS and injected subcutaneously into the right flank of mice or bilaterally (per flank). For tumor growth profile analysis, 0.5x10^{6} cells were suspended in 100 μL DPBS and injected subcutaneously into the right flank of mice. Tumor size was expressed by measuring the longest diameter (length) and its perpendicular (width) with a hand caliper. Blinding could not be applied during measurements. For actDC depletion in *Itgax*^{Cre} *Ccr7*$^{LSL\text{-}DTR}$ mice, mice were injected intraperitoneally with 200ng of diphtheria toxin (DT, Sigma-Aldrich) on the day of cancer cell injection, unless stated otherwise, and subsequently dosed with 100 ng of DT every three days for a two-week period. Blood samples from transgenic mice were analyzed via flow cytometry (for method see below) 16h after DT administration and animals with off-target recombination (based on complete lack of circulating B cells and T cells) were excluded from the study. For dual ICB treatment, mice were injected intraperitoneally with 200 μg of αPD-1 (RMP1-14, Bio X Cell) and 100 μg of αCTLA-4 (9D9, Bio X Cell) antibody twice weekly for 6 doses. Treatment was initiated at day 5 post tumor cell injection, when tumors were approximately 80-90 mm^{3} in size. For CD4^{+} T cell depletion, mice were injected intraperitoneally with αCD4 antibody (200 μg, clone GK1.5, Bio X Cell) one day prior to and three days after cancer cell injection. To block lymphocyte egress from LNs, FTY720 (20 μg per mouse, Sigma-Aldrich) was injected intraperitoneally in 100 μl saline approximately 1-2 hours prior to ACT followed by daily administration for seven consecutive days. In immune-competent mice, treatment was initiated either at day 0 or day 5 following 5555^{OVA} tumor cell implantation and continued daily for seven consecutive days.

Flow cytometry

For flow cytometry analysis, tissues (tumor, axillary and inguinal lymph node, lung, thymus) were harvested, cut into small pieces with scissors and incubated in RPMI containing 200 U/mL Collagenase IV (Worthington Biochemical) and 0.2 mg/mL DNase I (Roche) for 30 min at 37°C. Digested tissue or spleen was ground and filtered through a 70 μm cell strainer, washed with RPMI and pelleted. In lung or spleen cell suspensions, RBCs were removed using an RBC lysis buffer (Sigma-Aldrich). Cell suspensions were resuspended in PBS and labeled using LIVE/DEAD Fixable Aqua Dead Cell 405nm staining (Invitrogen) to define cell viability. Samples were rinsed in FACS buffer (PBS containing 1-2% FBS and 0.01% sodium azide) and incubated with combinations of the following antibodies: CD45 (30-F11), CD45.1 (A20), CD45.2 (104), B220 (RA3-6B2), CD19 (1D3), CD64 (X54-5/7.1), F4/80 (BM8), Gr-1 (RB6-8C5), CD63 (NVG-2), Ly6C (AL-21), Ly6G (1A8), H-2K^{b}/H-2D^{b} (28-8-6), MHC-II I-A/I-E (M5/114.15.2), CD11c (N418), CD11b (M1/70), XCR1

(ZET), CD103 (2E7), Sirpα (P84), CD40 (3/23), PD-L1 (MIH5 or 10F.9G2), PD-L2 (TY25), CD3ε (145-2C11), CD4 (RM4-5), CD8α (53-6.7), CD86 (GL-1), H-2K^{b}-SIINFEKL (25-D1.16), CD80 (16-10A1), CD69 (H1.2F3), CD25 (PC61.5), PD-1 (29F.1A12), CD44 (IM7), CD62L (MEL-14), LAG3 (eBioC9B7W), CD39 (Duha59), 2B4 (eBio244F4), TIGIT (1G9) or NK1.1 (PK136) from BD Biosciences, eBioscience or BioLegend, for 30min at 4°C. The anti-Fc Receptor (anti-CD16/32) antibody (39, eBioscience) was used to prevent non-specific binding. For chemokine receptor staining, cells were resuspended in 50 μL of complete RPMI with Brefeldin A (eBioscience), anti-Fc receptor antibody and anti-CCR7 antibody (4B12, BioLegend) and incubated for 25 min at 37°C. To determine cytokine and granzyme B levels, cell suspensions stained for extracellular markers were fixed and permeabilized using the IC Fixation and Permeabilization buffer set (eBioscience) according to the manufacturer's instructions. Cells were then resuspended in Permeabilization buffer and incubated with 2% normal rat serum (Invitrogen) for 15min and anti-IL12p40 (C15.6, BioLegend), anti-IFNγ (XMG1.2, Invitrogen), anti-TNFα (MP6-XT22, eBioscience) or anti-granzyme B (GB11, BD Biosciences) antibody for at least 30min at room temperature. A mix of Monensin – Brefeldin A (eBioscience) was added to cell suspensions 2-3h prior staining, to inhibit secretion of cytokines from the Golgi complex. For IFNγ and granzyme B staining in tumors and tdLNs, cell suspensions were also re-stimulated *ex vivo* with SIINFEKL (1 μg/mL) for 4-5 hours prior staining for flow cytometry. For nuclear protein staining, cell suspensions stained for surface markers were fixed and permeabilised using the Foxp3/Transcription Factor Staining Buffer Set kit (eBioscience) according to the manufacturer's instructions. Cells were then resuspended in Permeabilisation buffer and incubated with 2% normal rat serum (Invitrogen) for 15 min and TCF-1/7 (C63D9, Cell Signaling Technology) or TOX (REA473, Miltenyi Biotec) for 30 min at room temperature. After washing, labeled cell populations were analyzed by NovoCyte 3000 or Novocyte Quanteon (Agilent Technologies) flow cytometer. Live cell counts were quantified from the acquisition of a fixed number of 10 μm latex beads (Beckman Coulter) mixed with a known volume of cell suspension.

Flow cytometry standard.fcs files were analyzed using FlowJo v10.10.1 (FlowJo, LCC). All flow cytometry histograms were normalised to "Modal". Frequencies of cell populations were calculated as "Freq. of Parent", unless stated otherwise. To generate t-distributed Stochastic Neighbour Embedding (t-SNE) plots from flow cytometry data of BMDC cultures in FlowJo (related to Figure 3D), FlowAI was applied for sample clean-up to remove artifacts related to time-dependent signal and flow rate alterations during sample acquisition. After cleaning, samples on the cDC gate (Live MHC-II^{+} B220^{-} XCR1^{+} cDC1s and CD11b^{+} cDC2s) were concatenated in one.fcs file using the "Concatenate Populations" function. The t-SNE analysis was then performed using FlowJo "t-SNE" plugin and the resulting two-dimensional t-SNE map was used to visualize clusters based on their multi-dimensional surface marker expression.

For imaging flow cytometry, BMDCs co-cultured with 5555 ZsGreen^{pos} cancer cells were prepared for standard flow cytometry analysis. Following staining, cells were washed twice to remove unbound antibodies, resuspended in 40 μL of FACS buffer and analyzed via the ImageStreamX Mk II cytometer (Luminex) at a 40x magnification. To gate on ZsGreen^{pos} BMDCs, we used as a negative control labeled BMDCs and ZsGreen^{pos} cancer cells mixed right before acquisition. Imaging flow cytometry standard.cif and.rif files were analyzed using the IDEAS 6.2 software (Amnis).

H&E and mScarlet-I microscopy

To visualize Scarlet^{pos} cDC1s across tissues, *Xcr1*$^{Cre\text{-}mTFP1}$*Ccr7*$^{LSL\text{-}mScarlet\text{-}I}$ mice were anesthetized with isoflurane until surgical plane and perfused with 4% paraformaldehyde (PFA) fixative (Thermo Fisher Scientific). Tissues were further fixed in 4% PFA at 4°C overnight, washed with PBS and dehydrated in 30% sucrose. Tissues were then embedded in OCT embedding medium and consecutive 7 μm cryosections were cut, fixed with 4% PFA for 15min, washed with PBS and stained with DAPI (Thermo Fisher Scientific) for 15min at room temperature. For antibody staining following Scarlet visualization, coverslips were removed and sections were further fixed in 10% casein, incubated with primary antibodies at 4°C overnight, and further stained with secondary antibodies the following day at room temperature for an hour. To assess tissue morphology, air-dried sections were fixed in 70% industrial denature alcohol (IDA) for 1 min, rehydrated in running water and stained with Gill's II haematoxylin (Thermo Fisher Scientific) for 30 sec, followed by bluing and counterstaining with eosin (Thermo Fisher Scientific) for 10 sec. Slides were rinsed, dehydrated through a graded ethanol series (70%, 90%, 99% ×3) and cleared in xylene. All slides were coverslipped using ProLong Gold Antifade Mountant (Invitrogen). The Olympus VS120-L100-W-12 (Olympus Corporation) was utilized to image under fluorescence illumination using a Lumencor SOLA LED light source and a fast filter wheel with the Olympus penta AHF-SPX-QSEM (DAPI, FITC, TRITC, Cy5 and Cy7) filter set. The objective lens to capture data was an Olympus UPLSAPO20x (NA 0.75). Negative controls of Scarlet signal were obtained by processing tissues from littermate controls lacking Cre recombinase.

Images were analyzed using the HALO v4.0.5107.407 software (Indica Labs). More specifically, images from the same section were registered, aligned using the landmark function and fused into a single multi-channel.TIFF file. For tumor sections, fused imaged were then manually annotated (no blinding) to exclude necrotic areas, folded tissue or regions with staining artifacts and analyzed using the Indica Labs – HighPlex FL v4.3.2 module. Spatial mapping and proximity analysis (0-150 μm distance range divided into 15 10-μm-wide bands) was carried out to assess the spatial relationships between different cell populations.

Transwell migration assay

To assess chemotactic capability, BMDCs at 1x10^{6} cells/mL were plated on top of 24-well 6.5mm transwell inserts (filter membrane with 5.0 μm pore size, Corning). Into the bottom of the lower chamber, CCL21 chemo-attractant (BioLegend) was added in DC medium at concentration of 100 ng/mL. Transwell inserts with plain DC medium were used to determine the migratory capacity of BMDC populations in the absence of chemokine signals. Cells were incubated for 2.5h at 37°C and migrated cells were harvested and stained for flow cytometry analysis as described above.

BMDC-cancer cell co-cultures

Cancer cells were seeded in 10cm Petri dishes under standard culture conditions. To increase expression of MHC-I surface molecules, B16 cancer cells were treated with 100 ng/mL of recombinant IFNγ overnight. At 80-90% confluency, cancer cells were harvested, added directly in day 9 BMDC cultures at 1:1 ratio and incubated overnight at 37°C. To avoid alterations on cell surface repertoire, cancer cells for co-culture experiments were always detached using an enzyme-free 2mM EDTA/DPBS solution. When indicated, day 9 BMDC monocultures were treated overnight at 37°C with either 1:2 (v/v) tumor cell CM, synthetic PGE2 (50 ng/mL), poly I:C (1 μg/mL) or LPS (100 ng/mL).

OVA-specific TCR transgenic CD8$^+$ T cell isolation

Spleens and skin-dLNs from CD45.1 OT-I *Rag1*$^{-/-}$ mice were isolated, ground and filtered twice through a 70 μm cell strainer. RBCs were removed using an RBC lysis buffer (Sigma-Aldrich). Splenic cell suspensions deriving from OT-I *Rag1*$^{-/-}$ mice were further purified using the naive CD8$^+$ T cell isolation kit (Miltenyi Biotec), according to the manufacturer's instructions. OT-I purity (above 98%) was confirmed by flow cytometry using CD8α (53-6.7) and CD44 (IM7). Naive OT-I cells were injected via the lateral tail vein (0.5-1x10^6 cells in 100 μL DPBS per mouse) into recipient CD45.2 mice. For antigen presentation assays (see below), OT-I cells were cultured in complete RPMI supplemented with 0.1% 2-mercaptoethanol and 1% MEM non-essential amino acids solution (Gibco).

Pre-activation of OT-I cells for adoptive transfer

To pre-activate OT-I cells, spleens and LNs of CD45.1$^+$ OT-I *Rag1*$^{-/-}$ mice were processed as described above. Single cell suspensions were cultured in 24-well plates at a concentration of 1x10^5 cells/mL, in complete RPMI supplemented with 0.1% 2-mercaptoethanol, 1% MEM non-essential amino acids solution (Gibco), 1mM pyruvate (Gibco), 10mM HEPES (Sigma-Aldrich) and OVA peptide (SIINFEKL, 1nM, InvivoGen) at 37°C. Recombinant mouse IL-2 (BioLegend) at a concentration of 15 ng/mL was added to the primary cultures on day 3. On day 5, cultures were used for adoptive transfer via the lateral tail vein (1x10^6 cells in 100 μL DPBS per mouse) into recipient *Rag1*$^{-/-}$ CD45.2 mice. OT-I activation was confirmed by flow cytometry using CD8α (536.7), CD44 (IM7), CD69 (H1.2F3) and CD25 (PC61.5).

Cell sorting for *ex vivo* and *in vitro* functional assays

To separate actDC and restDC populations, tdLNs or BMDC-cancer cell co-cultures were harvested and processed for standard flow cytometry analysis as described above. FACS buffer for sorting experiments did not contain sodium azide. After washing, cell suspensions were filtered through a 70 μm cell strainer and sorted on a BD FACSAria III or BD FACSMelody with ≥98% purity. Sorted single cells were counted and ≥90% viability was confirmed through Türk's solution exclusion. To assess T cell proliferation, OT-I cells were stained using the CellTrace Violet Cell Proliferation Kit (ThermoFisher Scientific) according to the manufacturer's instructions and plated with cDC populations at different ratios (cDC:OT-I 1:9, 1:3, or 1:1) for 72h at 37°C. Naive OT-I cells and OT-I cells cultured with BMDCs and SIINFEKL peptide (1nM, InvivoGen) were used as a negative and positive control of T cell expansion, respectively. For pattern recognition receptor stimulation, CpG ODN 1668 (InvivoGen) was added to cDC:OT-I co-cultures at a concentration of 1 μg/mL.

H-2K^b-SIINFEKL multimer staining

To identify tumor-reactive CD8$^+$ T cells, 50 μL of peripheral blood were collected from tumor-bearing mice through tail vein bleeding. RBCs were removed using ACK lysing buffer (Gibco). Remaining cell suspensions were then washed and labeled using LIVE/DEAD Fixable Aqua Dead Cell 405nm staining (Invitrogen) to define cell viability. Samples were rinsed in FACS buffer and incubated with H-2K^b-SIINFEKL pentamer (ProImmune) or tetramer (Baylor College of Medicine) for 30min at room temperature. Samples were stained for extracellular markers and analyzed by flow cytometry.

Single-cell RNA sequencing and transcriptomic analysis of 5555 or CT26 tumors

For single-cell RNA sequencing, 5555[74] and CT26 tumors were processed for standard flow cytometry analysis (multiple tumors per group) as described above. Live CD45$^+$ cell suspensions were sorted on a BD FACSAria III with ≥98% purity. Sorted single cells were counted and ≥90% viability was confirmed through Trypan Blue exclusion. 16-18,000 cells + ~3.5% spike-in (of each 5555 melanoma sample) or 25,000 cells (of each CT26 tumor sample) were loaded into a channel of the Chromium Chip B (10x Genomics, PN-1000073). Single cell gel beads-in-emulsion (GEMs) were generated using the Chromium Controller and sequencing libraries prepared using the Chromium Single Cell 3' GEM, Library & Gel Bead Kit v3 (10x Genomics), according to the manufacturer's protocol.

Libraries were quality checked using the Agilent Bioanalyzer and quantified by qPCR using a KAPA Library Quantification Kit for Illumina Platforms (Roche). Paired-end sequencing was performed on an Illumina NextSeq 500 in High Output mode with an input of 1.4pM (5555) or 1.6pM (CT26).

Pre-processing (quality control (QC), alignment and initial filtering for empty droplets) of raw sequencing files was performed using the Cell Ranger v3.0.2 (10x Genomics). Output files (either the filtered_feature_bc_matrix.h5 file or the barcodes.tsv, features.tsv and matrix.mtx files) were imported on Partek Flow software (Single cell Toolkit, build version 12.3.0) for analysis. Single cell counts were then filtered for total read counts, % mitochondrial counts, % ribosomal counts and detected genes. Genes that were not expressed by any cell in the datasets were excluded. Following Log2(CPM+1) normalization, principal component (PC) analysis (PCA) was applied on filtered counts for dimensionality reduction and graph-based clustering was performed using the optimal PC number

defined by Scree plot. Clusters were then visualized through t-SNE and classified based on standard immune cell-specific biomarkers (Table S1). To infer RNA velocity analysis, unspliced and spliced counts are estimated from loom files generated from binary alignment map (BAM) files with Velocyto v0.17.25 package.[81] We used the same gene model, which was included with the Cell Ranger reference data ''refdata-cellranger-mm10-3.0.0''. The principal tree of annotated DC cluster subsets in low dimension is obtained from the DDTree (Partek Flow) and intersected with loom files for the combined velocity and transition matrix calculation using scanpy v1.10.1.[80] Cells were filtered for unspliced and spliced counts (using the default 20, ensuring genes had both at least 20 spliced and unspliced counts) and normalized using the method implemented in scVelo v0.3.2.[82] A KNN graph was calculated in scanpy with Neighbors set to 30, with 15 and 30 PCs used for downstream analyses in 5555 melanoma and CT26 colorectal cancer datasets, respectively. Data from scVelo's dynamic model were combined with transcriptional similarity matrices obtained from CellRank[78] to produce a combined kernel to infer RNA velocity on top of pre-computed dimensionality reductions. All RNA velocity analyses were performed using Python v3.10.12. Gene regulatory network analysis to identify actDC-specific regulons was performed with PySCENIC v0.12.1[79,89] against the 2022 mc_v10_clust cisTarget databases.

Single cell RNA sequencing and transcriptomic analysis of *in vitro* cultures

BMDCs cultured in the absence or presence of 5555 melanoma cells were processed for standard flow cytometry analysis and live CD45$^+$ cells were sorted with $\geq$98% purity as described above. To account for biological variability, we processed and pooled BMDC cultures deriving from two mice per culture condition. Sorted single cells were counted and $\geq$90% viability was confirmed through Trypan Blue exclusion. BMDC conditions were combined following cell hashing with the oligoconjugated TotalSeq™-A anti-mouse hashtag 6 (unstimulated), 7 (+ *Ptgs*$^{+/+}$ 5555) and 8 (+ *Ptgs*$^{-/-}$ 5555) antibodies (BioLegend). 30,000 cells were loaded into a channel of the Chromium Next GEM Chip G (10x Genomics, PN-1000120). Single cell GEMs were generated using the Chromium Controller and Chromium Next GEM Single Cell 3' Kit v3.1 (10x Genomics) according to the manufacturer's protocol. Gene expression and TotalSeq-A HTO libraries were produced according to the BioLegend TotalSeq-A protocol and 10x Genomics user guide.

Libraries were quality checked using the Agilent Bioanalyzer and quantified by qPCR using a KAPA Library Quantification Kit for Illumina Platforms (Roche). Paired-end sequencing was performed on an Illumina NovaSeq 6000 with XP loading and inputs of 0.9 (GEx library) and 1.8pM (HTO library).

Pre-processing using Cell Ranger, and filtering, normalization and exploratory analysis using Partek software was performed as described above. Hashtag demultiplexing was applied on BMDC counts after CLR normalization to specify culture conditions. Classification of DC clusters based on immune-cell-specific biomarkers is available on Table S1. To identify DC sub-populations, differential genes between the cDC1 and cDC2 clusters (identified via Wilcoxon Rank-Sum test where adjusted p value<0.05) were used as an input to highly variable gene selection, PCA and Leiden-based clustering in Seurat v5.3.1.[77] Clustering and UMAP generation were performed using the top 10 PCs and clustering was performed at a resolution of 0.5. To further characterise dendritic sub-populations, cDC1-related gene sets identified by Cheema et al.[36] were scored using Seurat module scoring.

QUANTIFICATION AND STATISTICAL ANALYSIS

Data are expressed as mean ± SEM, or mean with individual biological replicates, as specified in figure legends. Unpaired or paired Student's t test, Log-rank (Mantel-Cox) test, one-way ANOVA followed by Tukey's multiple comparison test, or two-way ANOVA followed by Šidák's multiple comparison test were used for data analysis. A p value<0.05 (*p<0.05, **p<0.01, ***p<0.001, ****p<0.0001) was considered significant. Statistics were calculated using GraphPad Prism v10.2.3 (GraphPad Software Inc). Partek Flow software, Python and R were used for analysis of single-cell RNA sequencing datasets.